Microscopy and Microanalysis (2019), **25**, 563–582
doi:10.1017/S1431927619000497

Microscopy AND Microanalysis

Review Article

Four-Dimensional Scanning Transmission Electron Microscopy (4D-STEM): From Scanning Nanodiffraction to Ptychography and Beyond

Colin Ophus*

National Center for Electron Microscopy, Molecular Foundry, Lawrence Berkeley National Laboratory, 1 Cyclotron Road, Berkeley, CA, USA

Abstract

Scanning transmission electron microscopy (STEM) is widely used for imaging, diffraction, and spectroscopy of materials down to atomic resolution. Recent advances in detector technology and computational methods have enabled many experiments that record a full image of the STEM probe for many probe positions, either in diffraction space or real space. In this paper, we review the use of these four-dimensional STEM experiments for virtual diffraction imaging, phase, orientation and strain mapping, measurements of medium-range order, thickness and tilt of samples, and phase contrast imaging methods, including differential phase contrast, ptychography, and others.

Key words: transmission electron microscopy (TEM), four dimensional-scanning transmission electron microscopy (4D-STEM), scanning electron nanodiffraction (SEND), nanobeam electron diffraction (NBED)

(Received 16 January 2019; revised 9 March 2019; accepted 19 March 2019)

Introduction

Transmission electron microscopy (TEM) is one of the most powerful characterization tools available to researchers studying nanoscale structures and phenomena. The unmatched spatial resolution of TEM, with the high degree of flexibility afforded by electromagnetic lenses and multipoles, and the large number of potential measurement channels have led to the development of many different operating modes for TEM. Scanning transmission electron microscopy (STEM), in particular, can perform a large number of different measurements, many of them simultaneously. This is because in STEM the electron probe is focused onto the sample surface and thus has a very small spatial extent, down to sub-atomic dimensions. After the STEM probe scatters from the sample, signals that can be measured include the forward diffracted electrons for various subsets of momenta, back-scattered electrons, X-rays, and secondary electrons generated inside the sample, and the energy loss spectroscopic signal. In this paper, we focus primarily on momentum-resolved measurements of the forward scattered electrons, especially those scattered elastically. Information on STEM development can be found in Pennycook & Nellist (2011) and other TEM textbooks.

Figure 1 shows a momentum-resolved STEM experimental dataset measured from a dichalcogenide two-dimensional (2D) material. The STEM probe is formed by TEM condenser optics and possibly aberration-corrected. Next, it is focused on the sample surface, where it propagates through and scatters. After exiting the sample, the probe is magnified and measured on the detector plane in the far field. Note that in Figure 1, the diffraction images are displaced from each other in order not to overlap, but in reality all images are measured at the same detector position.

Each image in Figure 1 is an average of 49 adjacent probe images (in a 7×7 grid), where each image is approximately four megapixels. This gives a total dataset size of 420 GB, recorded in 164 s. Large-scale four-dimensional (4D)-STEM experiments such as this one have become possible because of two developments: high speed and efficient direct electron detectors, and the widespread availability of computational power.

The name "4D-STEM" refers to recording 2D images of a converged electron probe, over a 2D grid of probe positions. The resulting datasets are 4D, hence the term 4D-STEM, by which we mean all forms of scattering measurements where 2D images of a STEM probe are recorded, either in real or diffraction space, for a 2D grid of probe positions. This paper will review many different forms of 4D-STEM measurements, their history, and some recent developments. We will also discuss naming conventions, electron detector development, and simulation of 4D-STEM datasets.

Basics of 4D-STEM

Naming Conventions

The name "4D-STEM" is widely used in the literature, for example in Ophus et al. (2014), Yang et al. (2015*a*), Ryll et al. (2016), Wang et al. (2018), Fatermans et al. (2018), Xu & LeBeau (2018), Hachtel et al. (2018), and Mahr et al. (2019), though this name is far from universal. Note that it has also been used in the past to refer to combination STEM electron energy loss spectroscopy (EELS) and tomography, which also produces a 4D dataset. This technique however is typically referred to as "4D-STEM-EELS," for

***Author for correspondence:** Colin Ophus, E-mail: cophus@gmail.com

Cite this article: Ophus C (2019) Four-Dimensional Scanning Transmission Electron Microscopy (4D-STEM): From Scanning Nanodiffraction to Ptychography and Beyond. *Microsc Microanal* **25**, 563–582. doi:10.1017/S1431927619000497

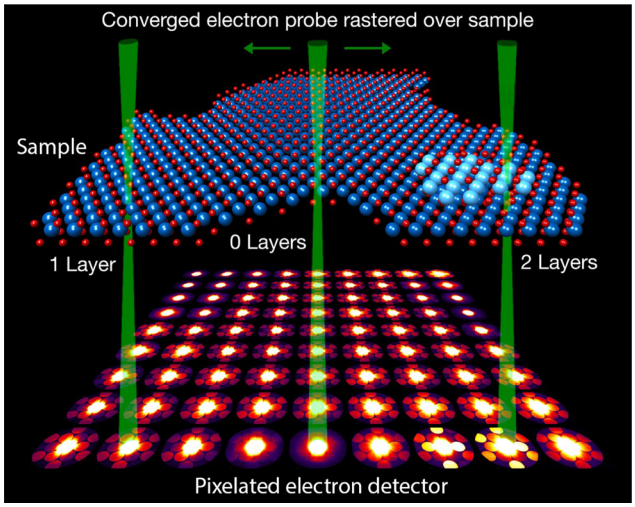

Fig. 1. Experimental 4D-STEM measurement of a dichalcogenide 2D material. Atomic map is inferred from the data, each diffraction pattern represents an average of 7 × 7 experimental images, green STEM probes are labeled for regions of the sample with one layer, vacuum, and two layers.

example in Jarausch et al. (2009), Florea et al. (2012), Goris et al. (2014), and Midgley & Thomas (2014). Related terms for images of STEM diffraction patterns in common use from the literature include "convergent beam electron diffraction" (CBED), "microdiffraction," "nanodiffraction," "diffraction imaging," and "diffractogram," all of which refer to diffraction images of a converged electron probe. The term "ronchigram" is named for the "Ronchi test" for measuring aberrations of telescope mirrors and other optical elements, developed by Ronchi (1964). STEM probe diffraction measurements of aberrations using periodic objects were introduced by Cowley & Spence (1979) and were referred to as ronchigrams by Cowley (1986). Today the term usually refers to a diffraction image that is nearly in focus, typically recorded from an amorphous material.

Some of the earliest experiments that could be classified as 4D-STEM in the sense of this paper were those performed by Zaluzec (2002) to measure the Lorentz deflection. Zaluzec referred to this method as "position resolved diffraction" (PRD) in accordance with earlier work where 2D diffraction patterns were recorded over a line scan. The term PRD is more often found in the X-ray diffraction literature, but can still be found in the TEM literature, for example in Chen et al. (2016). The similar term "spatially resolved diffractometry" was also used by Kimoto & Ishizuka (2011), which they used to refer to virtual imaging in 4D-STEM. The term "momentum-resolved STEM" is also used by some authors, for example Müller-Caspary et al. (2018*a*).

Perhaps the most common alternative name for a 4D-STEM measurement in diffraction space is "scanning electron nanodiffraction", used by Tao et al. (2009), Liu et al. (2013), Gallagher-Jones et al. (2019), and many others. A similar descriptor used in many studies is "nanobeam electron diffraction" (NBED), used for example by Clément et al. (2004), Hirata et al. (2011), and Ozdol et al. (2015). The term "pixelated STEM" can also be found in the literature, for example in MacArthur et al. (2013). In addition to referring to pixelated STEM, Hachtel et al. (2018) also introduced the term "universal detector" to refer to virtual imaging in 4D-STEM.

One 4D-STEM application discussed extensively below is crystal orientation mapping. When using computer image processing methods to classify the crystal orientations automatically, this method is called "automated crystal orientation mapping" (ACOM), for example in Schwarzer & Sukkau (1998), Seyring et al. (2011), Kobler et al. (2013), Izadi et al. (2017), and others.

Conventional STEM detectors record one value per pixel and usually have an annular (ring or circular) geometry. Common imaging modes include bright field (BF) where the detector is aligned with all or part of the unscattered probe, annular bright field (ABF) where a circle is removed from the center of the detector, and annular dark field (ADF) which selects an angular range of electrons scattered outside of the initial STEM probe. A very common STEM imaging mode is high-angle ADF (HAADF), which records only the incoherent signal of the thermal diffuse scattering (TDS) electrons, due to its easy interpretation (Pennycook & Nellist, 2011).

In this manuscript, we have chosen to use the general term of 4D-STEM in order to include imaging methodologies where the probe is recorded in real space, for example in (Nellist et al., 2006; Zaluzec, 2007; Etheridge et al., 2011).

Detector Development

The rise of popularity for 4D-STEM measurements is directly linked to the availability of high performance electron detector technology. Conventional STEM detectors for BF, ABF, ADF, and HAADF record only a single value per STEM probe position, and segmented detectors with 4–16 channels are used for differential measurements (Haider et al., 1994). Currently, the most common detector configuration recording full images in TEM is a charge coupled device (CCD) with digital readout, coupled with a scintillator, such as in Fan & Ellisman (1993) and De Ruijter (1995). These detectors have good electron sensitivity, but typically have readout speeds limited to video rate (≤60 frames/s) and limited dynamic range. This makes CCDs ill-suited to 4D-STEM diffraction imaging, which requires readout speeds comparable with the STEM probe scanning rate (μs to ms timescales) and the ability to measure high-intensity signals such as the BF disk and low-intensity signals such as the high-angle scattered electrons simultaneously.

There are two primary routes to building detectors more suitable for 4D-STEM applications. The first detector type is monolithic active pixel sensors (APS), which are complementary metal–oxide–semiconductor (CMOS) chips with a sensitive doped epitaxial layer. When high energy electrons pass through this layer, many low energy electrons are generated, which diffuse toward sensor diodes where they are collected and read out using CMOS electronics, as described in Mendis et al. (1997), Dierickx et al. (1997), and Milazzo et al. (2005). APS direct electron detectors have seen widespread deployment after being commercialized by several companies, for example in Ryll et al. (2016). See McMullan et al. (2014) for a performance comparison. APS detectors have very high sensitivities and fast readout speed, but relatively poor dynamic range. For high efficiency imaging, single "electron counting" is typically applied to images recorded with APS detectors (Li et al., 2013). This requires many pixels and relatively low electron doses in order to reduce the electron density recorded in each image to roughly less than 0.1 electrons per pixel per frame, since high densities prevent localization of individual electron strikes. If these conditions are met, electron counting can maximize the efficiency of 4D-STEM experiments, see Gallagher-Jones et al. (2019) for example. Note that because the design of APS detector pixels is relatively simple, these detectors typically contain a large number of pixels which decreases the electron density in each pixel.

https://doi.org/10.1017/S1431927619000497 Published online by Cambridge University Press

The second kind of detector used in modern 4D-STEM experiments is a hybrid pixel array detector (PAD). In this type of detector, an array of photodiodes is bump bonded to an application-specific integrated circuit, described in Ansari et al. (1989), Ercan et al. (2006), and Caswell et al. 2009). PADs have been optimized for 4D-STEM experiments by using high-gain integration and counting circuitry in each pixel, giving single electron sensitivity, high dynamic range, and fast readout speeds (Tate et al., 2016). This detector has also been commercialized and used for many 4D-STEM experiments, for example in Jiang et al. (2018).

Computational Methods

Almost every study described in this review uses computational imaging in some capacity. The digital recording of microscopy images and diffraction patterns quickly replaced the previously used film technology in no small part because it made it easy to use computers to analyze the resulting data. This review will not explicitly cover data recording, processing, and analysis methods. Instead we will provide a non-exhaustive list of code repositories that are currently being developed for 4D-STEM data analysis. These include: HyperSpy, pyXem, LiberTEM, Pycroscopy and py4DSTEM. Because so many of the 4D-STEM methods and technologies shown in this paper are being actively developed, we expect the software landscape to change considerably in the near future. We also want to encourage the vendors of commercial electron microscopes and detectors to allow full programmatic control of instrumentation in order to implement and optimize 4D-STEM experiments, and to use open source file formats for data and metadata.

Precession Electron Diffraction

Diffraction patterns from thicker samples can contain significant multiple scattering (i.e., dynamical diffraction). This leads to diffraction patterns where the average intensities of the Bragg disks are very uniform (i.e., structure factor details are lost), and a significant amount of fine structure generated inside each disk. Both of these effects can make indexing and quantitative intensity measurements of Bragg spots more difficult. One method to minimize multiple scattering is to collect an average diffraction pattern from many incident beam tilt directions, which is called "precession electron diffraction" (PED), or scanning-PED. Introduced by Vincent & Midgley (1994), PED uses deflection coils above and below the sample in order to tilt the angle of the beam incident on the sample, and then precess the beam through a range of azimuthal tilts. This "hollow cone" illumination integrates over excitation errors of different beams, which somewhat reduces dynamical scattering effects, and has found widespread application in electron crystallography (Midgley & Eggeman, 2015). As will be shown below, PED has been applied to many different 4D-STEM measurements. When combined with NBED measurements, this technique is sometimes referred to as "nanobeam precession electron diffraction", as in Rouviere et al. (2013).

Structure and Property Measurements

Virtual Imaging and Structure Classification

One of the most obvious uses of 4D-STEM diffraction imaging is the ability to use arbitrary "virtual" detectors by adding (or subtracting) some subset of the pixels in the diffraction patterns at each probe location. This removes one of the weaknesses of conventional STEM imaging; namely that a small number of bright and dark field detectors must be physically positioned at some angle from the optical axis, and cannot be changed relative to each other during the measurements. After a conventional STEM measurement, electrons within the scattering range are grouped together and can no longer be further separated by scattering angle. Note that nanodiffraction has been used for materials science investigations for a long time (Cowley, 1996). However, here we will review only 4D-STEM virtual imaging experiments, i.e., the sort of position-resolved nanodiffraction studies suggested by Zaluzec (2003) or shown experimentally such as Fundenberger et al. (2003), Lupini et al. (2015), and (Fatermans et al. (2018), and those which use such images to perform structural classification as in the schematic plotted in Figure 2a.

Figure 2 shows a 4D-STEM experiment imaging Y-doped ZrO_2 performed by Watanabe & Williams (2007). Two methods to interpret such a measurement are both shown: either selecting diffraction patterns from different regions of constant contrast over the probe positions in real space, or generating a virtual detector from subsets of pixels in the reciprocal space diffraction pattern coordinate system. A similar experiment was performed by Schaffer et al. (2008), where first virtual dark field images were formed from regions of interest in the real space image along an interface. Then, virtual detectors were applied to resulting spots in the diffraction patterns to form improved dark field images and combined into a single RGB color map. Tao et al. (2009) used a similar approach, shown in Figure 2c, to map out the positions of a nanoscale precipitate phase in $La_{0.55}Ca_{0.45}MnO_3$ as a function of sample temperature, using superlattice reflections. Zhang et al. (2017) have also performed phase mapping of beam-sensitive battery cathode materials using diffraction mapping.

Advancing detector technology and increased stability of TEM instruments and sample stages has led to continual improvement in 4D-STEM diffraction mapping. Figure 2d shows the complex microstructure of a nanocrystalline copper sample mapped by Caswell et al. (2009) using both diffraction spot orientation mapping and correlation of adjacent diffraction patterns. Diffraction mapping at atomic resolution was demonstrated by Kimoto & Ishizuka (2011), who recorded diffraction patterns from individual atomic columns in SrTiO3. Diffraction mapping capability with full control of the beam tilts before and after the sample was demonstrated by Koch et al. (2012). Jones & Nellist (2013) discussed the use of virtual detectors for imaging in 4D-STEM.

Figure 2e shows both virtual detectors in real space and diffraction space of a 4D-STEM measurement of an Fe–Al–Ni–Cr alloy measured by Gammer et al. (2015). Zeng et al. (2015) used nanodiffraction mapping to characterize residual MoS_2 products from nanosheets, after an electrochemical reaction in a liquid cell. Figure 2f shows virtual detectors applied to measure presence of three ordering variants of a battery cathode material by Shukla et al. (2016). This example shows how 4D-STEM can in many cases obtain the same information as atomic-resolution HRTEM or conventional STEM images, but over a far larger field of view (FOV), a method used again in Shukla et al. (2018). An example of virtual annular detectors is shown in Figure 2g, from an experiment by (Hachtel et al., 2018) imaging a DyScO3 sample at atomic resolution. Wang et al. (2018) have proposed methods for correcting sample drift both in STEM-EELS and 4D-STEM experiments. Li et al. (2019) have used machine learning methods to extract atomic-resolution defect information from 4D-STEM datasets.

https://doi.org/10.1017/S1431927619000497 Published online by Cambridge University Press

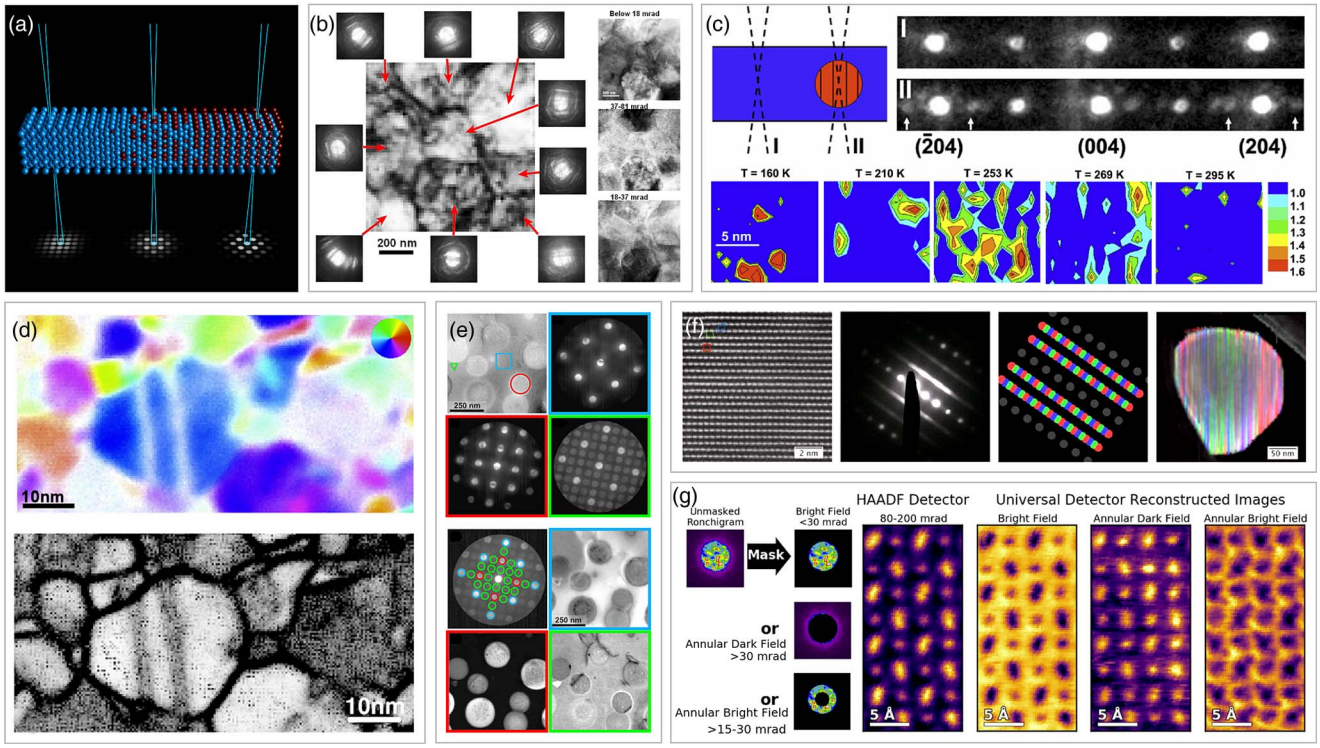

Fig. 2. Virtual imaging and classification in 4D-STEM. **a:** Schematic showing how properties such as local ordering can be directly determined from diffraction patterns. **b:** 4D-STEM experiment of Y-doped ZrO_2 from Watanabe & Williams (2007), showing both diffraction patterns from different probe positions and images generated from virtual detectors in diffraction space. **c:** Nanoscale precipitate phase in $La_{0.55}Ca_{0.45}MnO_3$ mapped from superlattice reflections, adapted from Tao et al. (2009). **d:** Top panel shows diffraction spot orientation and bottom panel shows correlation between adjacent diffraction patterns for a nanocrystalline Cu sample, adapted from Caswell et al. (2009). **e:** Top panel shows mean diffraction patterns from ROIs in real space, bottom panel shows virtual images generated from ROIs in diffraction space, from Gammer et al. (2015). **f:** Images from left-to-right are an HRTEM image of cathode material at atomic resolution showing three stacking variants, mean diffraction pattern, virtual detectors, and output RGB image showing outputs of virtual detectors, from Shukla et al. (2016). **g:** Virtual annular detectors at atomic resolution for a $DyScO_3$ sample, from Hachtel et al. 2018).

More exotic property measurements are also possible with 4D-STEM experiments. Wehmeyer et al. (2018) used virtual apertures to measure thermal diffuse scattering between Bragg disks as a measurement of local temperature. Tao et al. (2016) used 4D-STEM to study electronic liquid–crystal phase transitions and their microscopic origin, and Hou et al. (2018) used it to measure the degree of crystallinity in metal–organic-frameworks (MOFs). We expect that as pixelated detectors fall in price and larger amounts of computational power are available at the microscope, virtual imaging will become a very common operating mode for 4D-STEM. Commercial software to automate crystallographic phase mapping is already available, see for example Rauch et al. (2010), combined with PED, which was described in a previous section of this paper. It has been used in various materials science studies, including, for example Brunetti et al. (2011), who used it to understand Li diffusion in battery materials.

Crystalline and Semicrystalline Orientation Mapping

An important subset of structure classification for materials science is orientation mapping, and so we discuss it separately here. Electron backscatter diffraction using scanning electron microscopy (SEM) is the most commonly employed method to measure 2D maps of orientation distributions in crystalline materials, reviewed in Wright et al. (2011). Schwarzer & Sukkau (1998) also reviewed ACOM methods for measuring maps of crystalline grain orientations in SEM and suggested their future applicability to TEM experiments in order to increase resolution of orientation maps. In TEM diffraction imaging, orientation of a crystalline sample can be determined by either fitting Kikuchi diffraction patterns (Kikuchi, 1928) plotted in Figure 3a, or by direct indexing of the scattered Bragg spots or disks (Schwarzer, 1990) as shown in Figure 3b. Bragg spot indexing in 4D-STEM is essentially a form of selected area diffraction, where the "area" selected is the region illuminated by the STEM probe. Both methods are qualitatively similar, but each has strengths and weaknesses. Generally, spot indexing is better for thinner specimens, while Kikuchi diffraction performs better for thicker samples (as formation of Kikuchi bands relies on a sufficient diffuse scattering being present). Additionally, the orientation precision tends to be higher for Kikuchi diffraction due to the sharpness of the features measured, but it can fail in regions of high local deformation when the line signal becomes too delocalized. See Zaefferer (2000), Zaefferer (2011), and Morawiec et al. (2014) for further information comparing these methods.

Early implementations of orientation mapping in TEM did not have the computer memory or disk space to record every diffraction pattern for later analysis. Instead, patterns were typically acquired and indexed online. An early implementation of orientation mapping using Kikuchi patterns was developed by Fundenberger et al. (2003). Figure 3c shows one of these measurements, how it is high pass filtered and then fitted with an indexed line pattern, and finally an output orientation map for a deformed aluminum sample. As shown in Figure 2b, Watanabe & Williams

https://doi.org/10.1017/S1431927619000497 Published online by Cambridge University Press

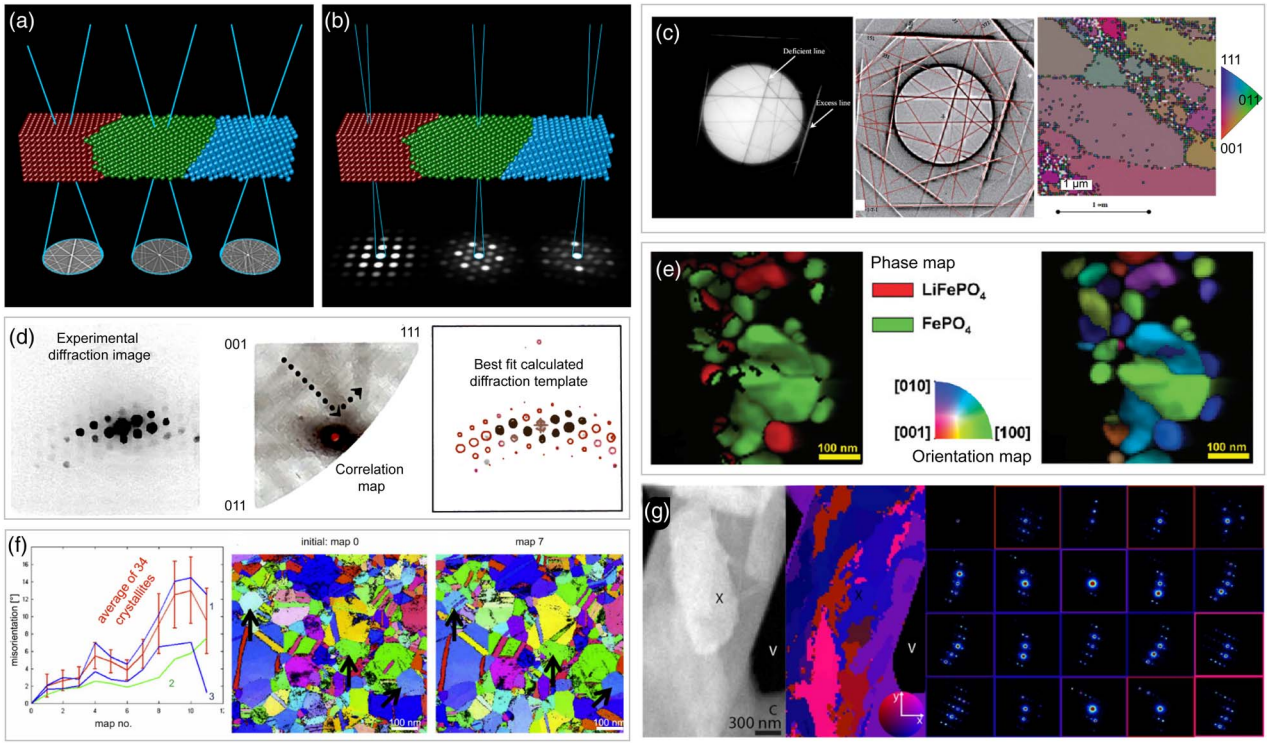

Fig. 3. Orientation mapping in 4D-STEM, using (**a**) Kikuchi patterns, or (**b**) Bragg disk diffraction. **c:** Kikuchi patterns indexing and orientation map of aluminum, adapted from Fundenberger et al. (2003). **d:** Orientation of Bragg disk pattern estimated with template matching, and resulting correlation scores for all orientations, by Rauch & Dupuy (2005). **e:** Simultaneous phase and orientation determination for $LiFePO_4$, from Brunetti et al. (2011). **f:** *In-situ* orientation mapping of nanocrystalline Au during a mechanical test, from Kobler et al. (2013). **g:** Orientation map of a biological peptide crystal, from Gallagher-Jones et al. (2019).

(2007) performed a very early 4D-STEM experiment where a Kikuchi diffraction orientation map could be constructed from a 4D-STEM scan. The Kikuchi method has been applied in many materials science studies, for example to a TiAl alloy by Dey et al. (2006), to cold-rolling of Ti by Bozzolo et al. (2007), to ferroelectric domains by MacLaren et al. (2010), and others. Note that Kikuchi pattern orientation mapping can also be performed in an SEM; this method has been demonstrated by Trimby (2012) and Brodusch et al. (2013).

An example of orientation mapping using Bragg spots is shown in Figure 3d from Rauch & Dupuy (2005). They introduced a fast "template matching" procedure, where the diffraction patterns are pre-computed for each orientation of a given material, and then, as shown in Figure 3d, a correlation score is computed for each experimental pattern. This method can be fully automated, and can also generate an estimate of the measurement confidence using the maximum correlation score (Rauch et al., 2010). Combined with PED, phase and orientation mapping has been commercialized and widely deployed (Darbal et al., 2012). A review of these methods for automated orientation mapping is given in Rauch & Véron (2014). The combination of scanning diffraction measurements, PED, and sample tilt to create 3D orientation tomographic reconstructions was shown by Eggeman et al. (2015). Other extensions to orientation mapping include applying principal component analysis and machine learning techniques to orientation measurements in 4D-STEM datasets, for example in studies by Sunde et al. (2018) and Ånes et al. (2018).

Figure 3e shows simultaneously recorded phase and orientation maps for LiFePO4, from an experiment performed by Brunetti et al. (2011) using PED and the spot matching method. These experiments were used to determine the correct transformation pathway model for this material, thus highlighting the usefulness of "plug and play" methods for TEM phase and orientation mapping. Kobler et al. (2013) extended ACOM experiments to *in-situ* mechanical testing measurements of nanocrystalline Au, with an example shown in Figure 3f. In this example, the misorientation angle of many grains was measured as a function of the loading force. These and many other statistics can be obtained simultaneously using time-resolved ACOM. Other examples of *in-situ* studies include: Idrissi et al. (2014), Garner et al. (2014), Bufford et al. 2015), Izadi et al. 2017), Guo & Thompson (2018), and others. An extreme example of orientation mapping was recently published by Bruma et al. (2016), who analyzed beam-induced rotation of 102-atom Au clusters.

Orientation maps can also be determined for semicrystalline materials, such as small molecule assemblies or polymers. One such example was shown by Panova et al. (2016), who mapped the degree of crystallinity and orientation of a polymer sample. Bustillo et al. (2017) extended this method to include multiple soft matter samples, including organic semiconductors. Mohammadi et al. (2017) have also performed orientation mapping of semiconducting polymers using 4D-STEM. They employed a statistical approach to measure the angular deviation of the $\pi - \pi$ stacking direction over a very large FOV. Orientation mapping has even been applied to peptide crystals, in the study by Gallagher-Jones et al. (2019) which analyzed small magnitude ripples, as shown in Figure 3g. The ability to use very low electron currents, small convergence angle (large real space probe size) or highly defocused STEM probes, and adjustable step size between adjacent measurements are key advantages of 4D-STEM mapping of radiation-sensitive materials. For such materials, the maximum obtainable spatial resolution can be achieved by careful tuning

https://doi.org/10.1017/S1431927619000497 Published online by Cambridge University Press

of the experimental parameters and dose in order to measure structural properties such as orientation to the required precision, balanced against the density of probe positions. For a review of electron beam damage mechanisms and how they can be minimized, we direct readers to Egerton (2019).

Strain Mapping

Many functional materials possess a large degree of local variation in lattice parameter (or for amorphous or semicrystalline materials, variation in local atomic spacing), which can have a large effect on the materials' electronic and mechanical properties. TEM can measure these local strains with both good precision and high resolution using CBED patterns, NBED, HRTEM, and dark field holography (Hÿtch & Minor, 2014). Strain measurements with CBED (or large angle CBED, i.e., LACBED) usually refers to using precision measurements of the higher order Laue zone (HOLZ) features of the diffraction pattern of a converged electron probe to directly probe the local lattice parameter (Jones et al., 1977). While in principle this is compatible with 4D-STEM measurements, these measurements typically require detailed calculations to interpret the CBED patterns (Rozeveld & Howe, 1993), samples thin enough for the kinematic approximation to hold (Zuo, 1992), and usually a favorable symmetry of the CBED pattern along the available sample orientations (Kaufman et al., 1986). Nevertheless, CBED HOLZ measurements of local strain are widely used, especially for single crystalline semiconductor samples such as in Clément et al. (2004) or Zhang et al. (2006).

In contrast, strain measurements from NBED experiments are usually simpler to interpret. Because the local strain precision does not depend on directly measuring the atomic column positions, the FOV is essentially unlimited and almost any sample and orientation can be used (Béché et al., 2009). A schematic of an NBED strain measurement is shown in Figure 4a, illustrating the inverse relationship between interatomic distance and diffraction disk spacing.

The NBED strain measurement technique was first introduced by Usuda et al. (2004), applied to the sample shown in Figure 4b. To improve the spatial resolution of the strain measurements, the STEM probe size must be decreased by opening up the convergence semiangle of the probe-forming aperture in diffraction space. This however will introduce unwanted fine structure contrast in the diffraction disks for thicker samples, due to excitation errors and dynamical diffraction, shown in experiments by Müller et al. (2012*a*) and plotted in Figure 4c. In that study, the authors focused on making their measurements as accurate and robust as possible for the large variation in the diffraction disk intensity patterns, using circular pattern recognition. This was also the focus of the work by Pekin et al. (2017), who analyzed using different correlation methods where a vacuum reference probe was compared with experimental and synthetic diffraction patterns. Other authors have analyzed the accuracy of NBED strain measurements including Williamson et al. (2015), Grieb et al. (2017), and Grieb et al. (2018), or the influence of artifacts such as elliptic distortion by Mahr et al. (2019).

Many researchers have applied NBED to materials science studies, including Liu et al. (2008), Sourty et al. (2009), Favia et al. (2010), Uesugi et al. (2011), and Haas et al. (2017). Very recent studies, including Han et al. (2018), have even extended strain measurements to heterostructures in very weakly scattering 2D materials. Comparisons of the strengths and weaknesses between NBED and other TEM strain measurement methods have been performed by Favia et al. (2011) and Cooper et al. (2016).

4D-STEM strain measurements have an inherent trade-off between resolution in real space and reciprocal space. A larger convergence angle will generate a smaller probe, giving better resolution in real space. However, this will also decrease the strain measurement precision. By decreasing the convergence angle, the STEM probe size in real space will be increased. A 4D-STEM measurement under these conditions will have lower spatial resolution but improved strain precision, due to averaging the strain measurement over a larger volume. However, the STEM probes can also be spaced further apart than the spatial resolution limit. Thus the only limit on FOV size is the speed of the detector readout. By using the millisecond readout times possible with direct electron detectors, the FOV can be increased as demonstrated by Müller et al. (2012*b*). Another example of the large FOV possible with 4D-STEM strain measurements is plotted in Figure 4d, by Ozdol et al. (2015). In this work, the sample region scanned was almost 1 μm^2, and the measurement was found to be extremely consistent across the FOV for a well-controlled multilayer semiconductor sample. 4D-STEM strain measurements have also been performed *in situ*, for example in Pekin et al. (2018).

One notable extension to NBED strain measurements in 4D-STEM is the use of PED to enhance the measurement precision. Heterogeneity in the diffraction disks is typically the limiting factor in the measurement precision, for example as shown in measurements by Pekin et al. (2017). PED can improve precision of 4D-STEM strain measurements, shown by Rouviere et al. (2013), Vigouroux et al. (2014), and Reisinger et al. (2016) for multilayer semiconductor devices. The improvement in precision for PED strain measurements was also analyzed in detail by Mahr et al. (2015). PED was also used to measure strain maps for complex polycrystalline materials by Rottmann & Hemker (2018), including high precision measurements of strain in low angle grain boundaries and even single dislocations. These experiments are shown in Figure 4e. Mahr et al. (2015) also proposed the use of a patterned probe-forming aperture to improve strain measurement precision, specifically the addition of a cross which divides the probe into four quarters. Guzzinati et al. (2019) have also used a patterned annular ring aperture to generate Bessel beam STEM probes, which improves the measure of strain precision.

In addition to crystalline materials, amorphous and semicrystalline materials can also exhibit local deviations away from the mean atomic spacing or average layer stacking distance respectively. Ebner et al. (2016) demonstrated that it was possible to measure this variation in a metallic glass. By combining this method with 4D-STEM performed with a fast detector, Gammer et al. (2018) were able to map the strain distribution in a metallic glass sample machined into a dogbone geometry for *in-situ* mechanical testing. Figure 4f shows an intermediate time step where the sample is under mechanical load; the mean CBED image shows the characteristic "amorphous ring" which was fit for every probe position to determine the relative strain maps, referenced to the unloaded sample.

Finally we note that alternative detector technologies have also been employed to measure strain maps. For example, Müller-Caspary et al. (2015) used a delay-line detector to map strain in field effect transistors fabricated from silicon.

Medium Range Order Measurement Using Fluctuation Electron Microscopy

Many interesting materials in materials science are not crystalline, and the tendency of some materials to form structurally disordered

https://doi.org/10.1017/S1431927619000497 Published online by Cambridge University Press

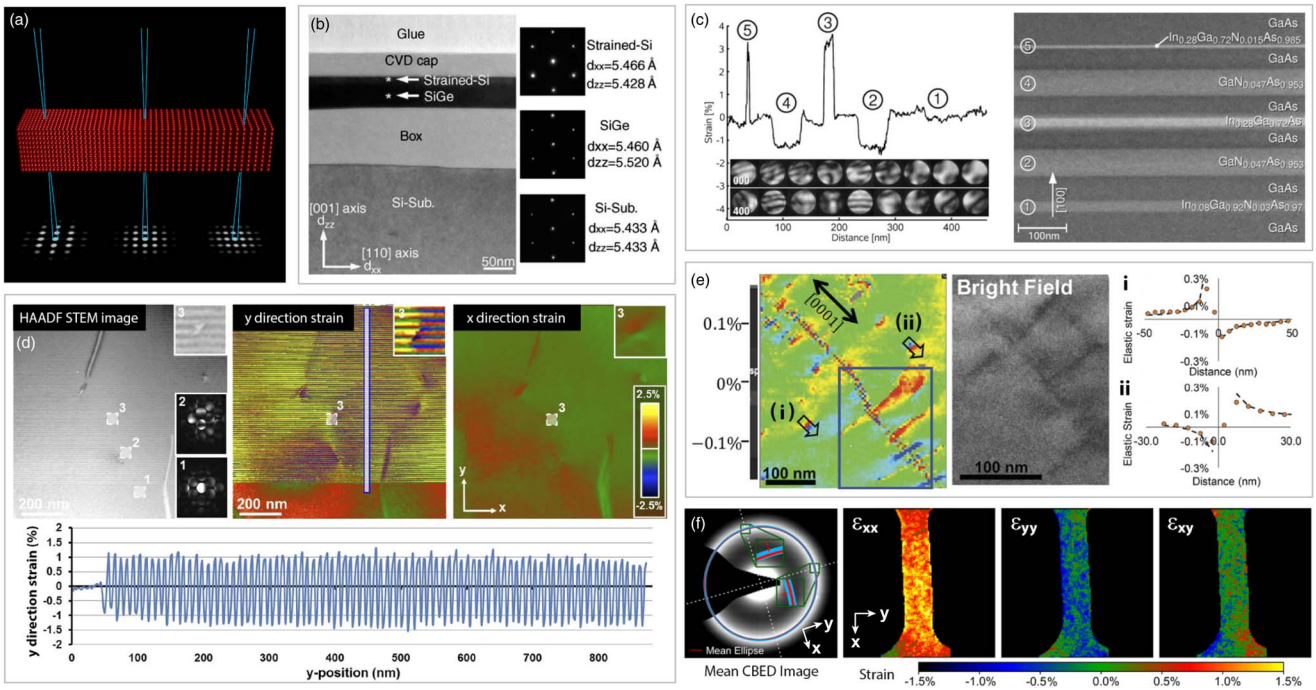

Fig. 4. Strain measurements in 4D-STEM. **a:** Schematic showing how diffraction disk spacing varies inversely with interatomic distances. **b:** Precise lattice parameter determination in multilayer semiconductor sample, from Usuda et al. (2004). **c:** Strain measurements in the presence of large variations of diffraction disk contrast patterns, adapted from Müller et al. (2012*a*). **d:** Strain maps with a large FOV, from Ozdol et al. (2015). **e:** Strain map from a polycrystalline sample, with strain distributions of single distributions plotted, from Rottmann & Hemker (2018). **f:** Strain measurements from a metallic glass mechanical testing sample, adapted from Gammer et al. (2018).

or "glassy" phases has been discussed for a long time (Phillips, 1979). The degree of medium range order (MRO) in glassy materials can be measured using "fluctuation electron microscopy" (FEM), as suggested by Treacy & Gibson (1996) and drawn schematically in Figure 5a. Figure 5b shows FEM measurements of α-Ge performed using converged electron probes, shown by Rodenburg (1999). This experiment demonstrates the basic principle of FEM: when the probe is focused to roughly the same length scale as the atomic ordering length of the sample, "speckles" appear in the diffraction pattern. When the probe is defocused (made larger in the sample plane), these speckles fade away. Measuring the intensity variance as a function of scattering angle (e.g., the ring shown in Fig. 5b) and probe size can yield information about the degree of MRO and the length scales where it is present in a sample. Voyles & Muller (2002) showed that STEM has significant measurement advantages over other TEM operating modes for FEM, one being the ability to easily adjust the probe size, for "variable resolution" (VR)-FEM. Some of their FEM measurements of α-Si are shown in Figure 5c. By using VR-FEM, the characteristic length scale of the MRO can be determined, such as in the example plotted in Figure 5d from Bogle et al. (2010). VR-FEM has been used to study many other materials, for example metallic glasses in Hwang et al. (2012) and α-Si in Hilke et al. (2019).

A large amount of scattering information is collected when performing a 4D-STEM FEM experiment. In addition to estimating the degree of MRO, it can also be used to measure the density of atomic clusters with different rotational symmetry. Examples of diffraction images of individual atomic clusters are shown in (Hirata et al., 2011). Figure 5e shows a measurement of Cu–Zr metallic glass where Liu et al. (2013) used angular cross-correlation functions of the diffraction patterns to measure the length scale and density of all rotational orders up to 12-fold symmetry. By comparing these measurements with atomic models, they concluded that icosahedral ordering was the dominant structural motif due to strong measurements of two, six, and tenfold symmetries. Figure 5e also shows spatial maps of these features. A follow up study by Liu et al. (2015) used simulations to test the interpretation of angular cross-correlation functions. Pekin et al. (2018) have extended this method to *in-situ* heating experiments for a Cu–Zr–Al metallic glass, and Im et al. (2018) have measured the degree of local ordering for different angular symmetries in a Zr–Co–Al glass, both using modern 4D-STEM cameras capable of recording a large amount of data with good statistics. A review of TEM measurements of heterogeneity in metallic glasses has been published by Tian & Volkert (2018).

Position-Averaged Convergent Beam Electron Diffraction

Quantitative CBED has a long history in TEM research, since under the right imaging conditions various sample parameters such as thickness can be determined with high precision (Steeds, 1979). However, conventional CBED experiments can require precise tilting of the sample, a minimum sample thickness to be effective, and sometimes require simulations to interpret the results. A recent related diffraction imaging method was introduced by LeBeau et al. (2009), called position-averaged convergent beam electron diffraction (PACBED). In this technique, shown schematically in Figure 6a, the diffraction patterns of an atomic-scale (large convergence angle) probe are incoherently averaged as the beam is scanned over the sample surface. As long as the averaging is performed over at least one full unit cell of a crystalline sample, PACBED images form a fingerprint signal, which can be used to determine sample parameters such as thickness, tilt, or sample

https://doi.org/10.1017/S1431927619000497 Published online by Cambridge University Press

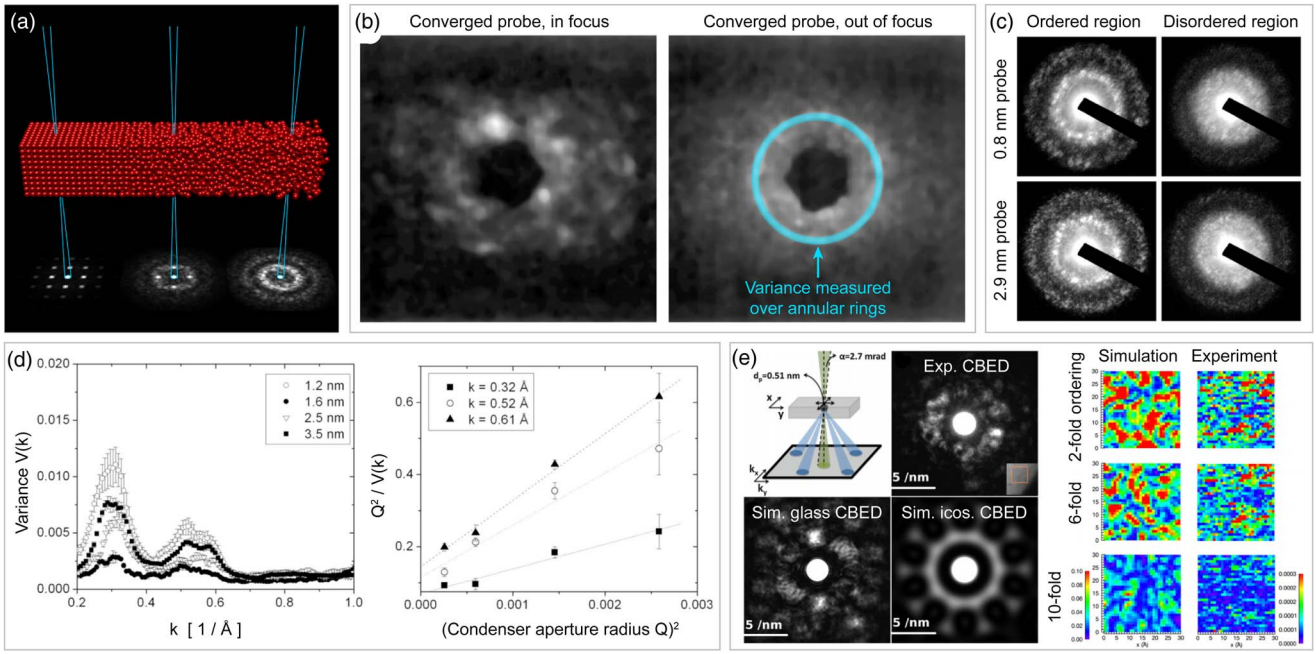

Fig. 5. FEM in STEM. **a:** Schematic showing how structural disorder generates the speckle pattern used in FEM. **b:** FEM measurements of α-Ge, adapted from Rodenburg (1999). **c:** FEM measurements of α-Si using a variable STEM probe size, from Voyles & Muller (2002). **d:** Characteristic length scale measurements of MRO in α-Si, from Bogle et al. (2010). **e:** Example of diffraction patterns of a Cu–Zr metallic glass, measurement of local MRO symmetry using angular cross-correlation functions, adapted from Liu et al. (2013).

polarization with high precision, by comparing directly with simulated PACBED images, as shown by LeBeau et al. (2010). Figure 6b shows one of their experiments, thickness determination of a $PbWO_4$ sample over a large range of sample thicknesses, using comparisons with Bloch wave simulations. PACBED thickness measurements have found widespread application in STEM experiments, for example in Zhu et al. (2012), Hwang et al. (2013), Yankovich et al. (2014), and Grimley et al. (2018).

Ophus et al. (2014) showed that 4D-STEM datasets of crystalline samples can be adapted to form PACBED images. First, the lattice is fit to either a simultaneously recorded ADF image, or a virtual image from the 4D-STEM dataset, and then each probe is assigned to a given unit cell. Averaging these patterns produces a single unit cell-scale PACBED image. An example of this procedure is shown in Figure 6c, where PACBED was used to determine the local composition of a $LaMnO_2$–$SrTiO_3$ multilayer stack in a STEM instrument without aberration correction, from Ophus et al. (2017*a*). Note that as seen in the HAADF images, the STEM probe resolution was not sufficient to resolve individual atomic columns inside the perovskite unit cell, showing that PACBED does not require high resolution STEM imaging. PACBED has also been used to measure unit cell distortion in double-unit-cell perovskites by Nord et al. (2018). A recently developed method to augment PACBED fitting was shown by Xu & LeBeau (2018), who used a convolutional neural network to automatically align and analyze the images. They showed that this approach can be quite robust to noise and can process PACBED images very quickly, which is important since the dataset sizes can be very large.

Phase Contrast Imaging

As described above, the most popular STEM imaging method for samples in materials science is HAADF measurements. However, HAADF is not very sensitive to weakly scattering samples such as low atomic number materials or 2D materials (Ophus et al., 2016). A more dose-efficient alternative is phase contrast imaging, which is therefore more suitable for these cases. Methods for measuring the phase shift imparted to an electron wave by a sample in a STEM experiment were first discussed by Rose (1974), Dekkers and De Lang (1974), and Rose (1977). These STEM phase contrast imaging methods and some modern 4D-STEM extensions will be discussed in this section.

Differential Phase Contrast

When a converged electron probe has a similar size to the length scale of the variations of a sample's electric field (gradient of the electrostatic potential), it will be partially or wholly deflected. Figure 7a shows an ideal probe deflection in the presence of a phase gradient with infinite extent. This momentum change imparted to the STEM probe can be measured in diffraction space using a variety of detector configurations, originally by using a difference signal between different segmented detectors that do not have rotational symmetry (Dekkers & De Lang, 1974), a method long known in optical microscopy (Françon, 1954). The differential phase contrast (DPC) imaging technique implemented on segmented detectors (Haider et al., 1994) was steadily improved all the way to atomic resolution imaging (Shibata et al., 2012). More information on the theory of DPC can be found in Lubk & Zweck (2015). Note that in Lorentz imaging modes in TEM, DPC measurements are also sensitive to the magnetic field of the sample (Chapman et al., 1990).

As discussed by Waddell & Chapman (1979), Pennycook et al. (2015), and Yang et al. (2015*b*), use of fixed segmented detectors for DPC measurements reduces the information transfer efficiency of many spatial frequencies. One way to avoid this problem is to perform a full 4D-STEM scan using a pixelated detector, and

https://doi.org/10.1017/S1431927619000497 Published online by Cambridge University Press

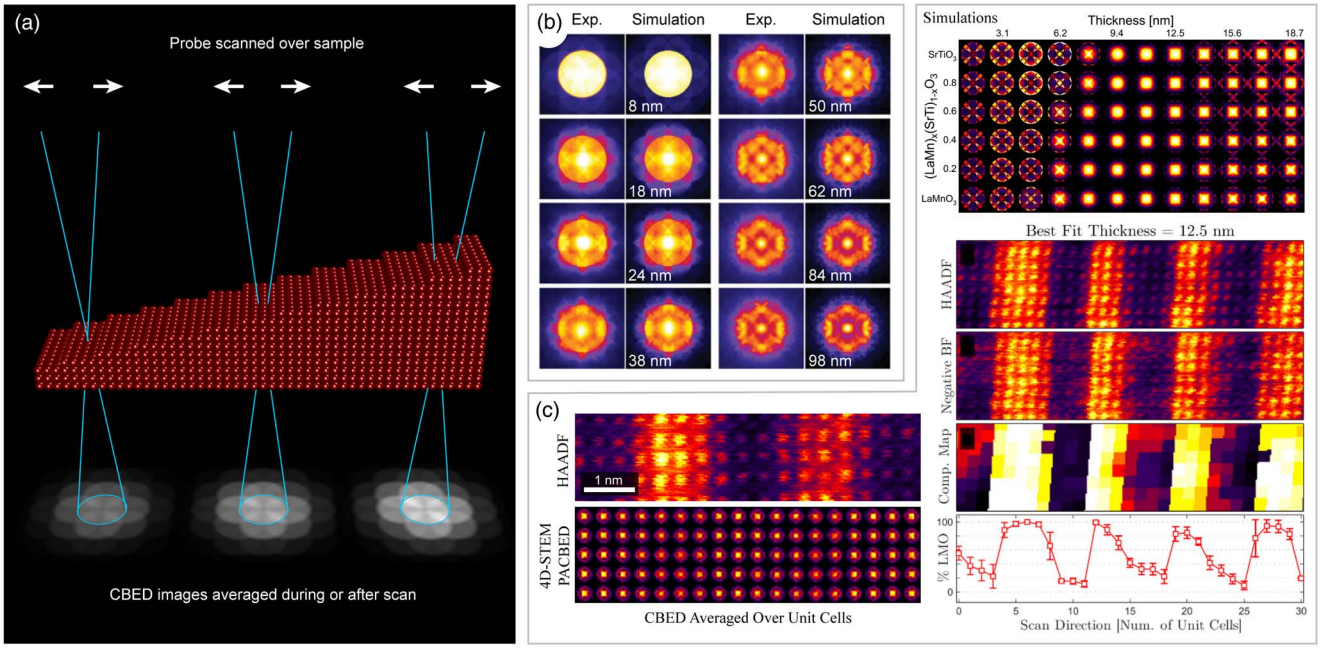

Fig. 6. Position averaged convergent beam electron diffraction (PACBED). **a:** Schematic showing how thickness strongly modules PACBED images. **b:** Thickness fitting of PbWO4 using PACBED, adapted from LeBeau et al. (2010). **c:** Composition fitting of $LaMnO_3$–$SrTiO_3$ multilayers using PACBED, adapted from Ophus et al. (2017*a*).

measuring the momentum change of the electron probe using a "center of mass" (COM) measurement over all pixels. Müller-Caspary et al. (2017) calculated that approximately 10×10 detector pixels were sufficient for COM DPC measurements, though more pixels may be desired for redundancy, or to perform additional simultaneous measurements such as HAADF imaging. They have also published a follow up study in Müller-Caspary et al. (2018*b*) to directly compare COM DPC with segmented detector DPC. Quantitative DPC can also be used for thicker samples if a large probe-forming aperture is combined with segmented detectors aligned with the edge of the probe as shown by Brown et al. (2019).

An early 4D-STEM DPC measurement of the Lorentz field deflection of a permalloy microdot by Zaluzec (2002) is plotted in Figure 7b. One of the first 4D-STEM measurements which measured the deflection of the STEM probe around atomic columns in $SrTiO_3$ was performed by Kimoto & Ishizuka (2011). These (x,y) STEM probe displacements around columns of Sr and Ti–O are plotted in Figure 7c. Since then, 4D-STEM DPC has been applied to various materials science problems. Some atomic-resolution examples include imaging of $SrTiO_3$ by Müller et al. (2014), imaging of GaN and graphene by Lazić et al. (2016), and imaging of $SrTiO_3$ and MoS_2 by Chen et al. (2016). Figure 7d shows a 4D-STEM DPC measurement of a multilayer $BiFeO_3$/$SrRuO_3$/$DyScO_3$ stack performed by Tate et al. (2016). Hachtel et al. (2018) measured octahedral tilts in the distorted perovskite $DyScO_3$, which are plotted in Figure 7e. These and other literature examples such as Krajnak et al. (2016), Nord et al. (2016), and Müller-Caspary et al. (2018*a*) show that 4D-STEM DPC is becoming a widespread tool for easy phase contrast measurements in STEM over a large range of length scales. Yadav et al. (2019) have recently shown that in addition to the local electric field, the local polarization can be measured simultaneously using 4D-STEM.

One advantage of DPC relative to more complex 4D-STEM measurements is that it reduces the measurement data of each probe to a very small number of variables such as the COM displacement vector. This allows fast alternatives to pixelated detectors to be used for DPC measurements, such as the previously mentioned segmented or delay-line detectors, or a duo-lateral position sensitive diode detector which can read out the COM of the probe as opposed to a full image, such as in Schwarzhuber et al. (2018). It may also be possible to use pixelated 4D-STEM detectors in combination with dedicated hardware directly after the detector pixels such as a field-programmable gate array, to perform simple measurements such as DPC (Johnson et al., 2018). This would remove the necessity of transferring, storing, and processing the full 4D-STEM datasets, which can be very large. A speed up in DPC inversion can also be accomplished computationally, as in Brown et al. (2016).

Ptychography

The DPC experiments described in the previous section reduce the measurement performed at each probe position to a two element vector corresponding to the mean change of the electron probe's momentum due to gradients in the sample potential. This is an intuitive and useful way to understand the beam–sample interactions due to elastic scattering in STEM, but discards a significant amount of information about the sample. This is because for thin specimens, STEM is essentially a convolution of the electron probe with the projected potential of a sample. By recording the full STEM probe diffraction pattern, we are measuring the degree of scattering for many different spatial frequencies of the sample's projected potential. Combining many such overlapping measurements such as the 4D-STEM experiment shown in Figure 8a, we can use computational methods to reconstruct both the complex electron probe and complex sample potential with high accuracy. Hegerl & Hoppe (1970) coined the name "ptychography" for this class of methods. The heart of this method was described in a series of papers, Hoppe (1969*a*),

https://doi.org/10.1017/S1431927619000497 Published online by Cambridge University Press

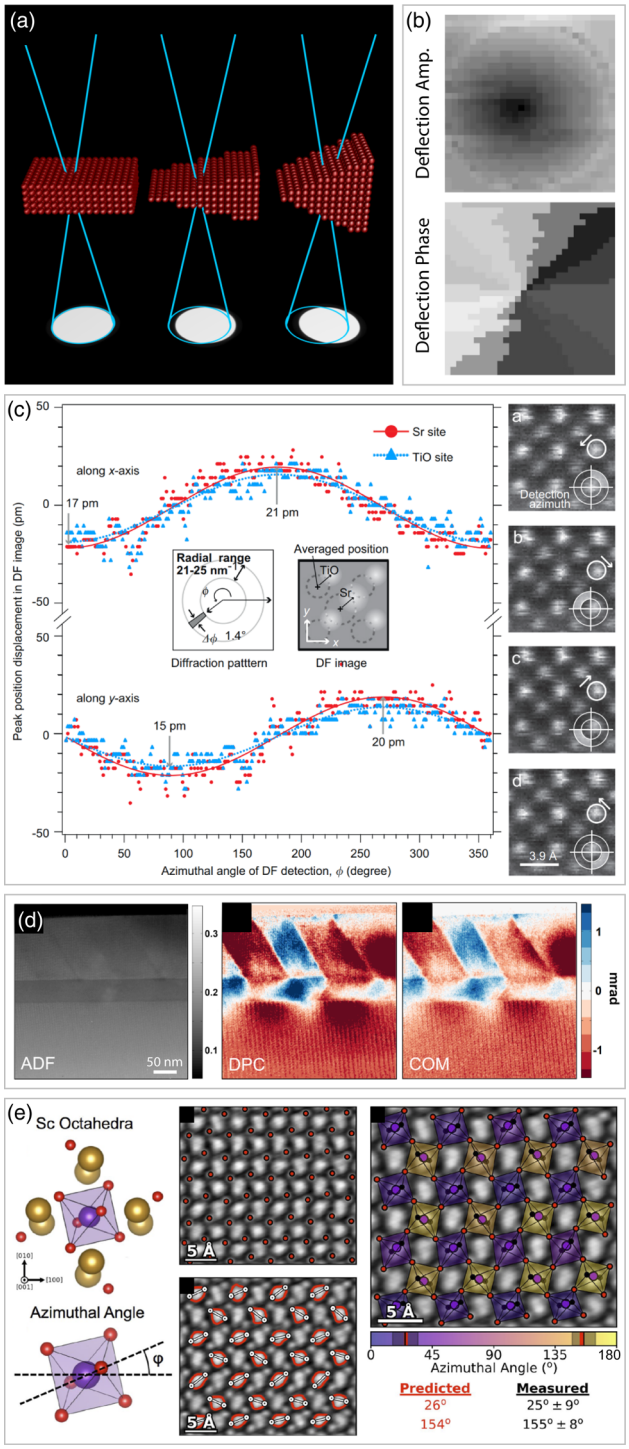

Fig. 7. DPC measurements in STEM. **a:** STEM probe deflection from ideal phase wedges with different slopes. **b:** Lorentz field deflection measurement of a permalloy microdot, adapted from Zaluzec (2002). **c:** Shift of peak positions in $SrTiO_3$, from Kimoto & Ishizuka (2011). **d:** Simultaneous measurements of ADF image, DPC signal from segments, and COM DPC signal from a multilayer stack, adapted from Tate et al. (2016). **e:** DPC measurements of octahedral tilts in $DyScO_3$, from Hachtel et al. (2018).

Hoppe & Strube (1969), and Hoppe (1969*b*). Figure 8b shows the essential idea of ptychography, where at different electron probe positions, there is substantial overlap in the illuminated regions. The differing intensities in these overlapping regions can be used to solve for the phase of the electron exit wave. The lattice diffraction images also shown in Figure 8b demonstrate the high sensitivity of diffraction images to the local alignment of the probe with respect to an underlying lattice.

Over the next two decades, a few theoretical studies of ptychography were published including Hawkes (1982) and Konnert & D'Antonio (1986), and also some experimental scanning microdiffraction studies including Cowley (1984) and Cowley & Ou (1989). However, the first reconstruction method for ptychography similar to modern methods has not been published to date (Bates & Rodenburg, 1989). These authors later published a substantially improved reconstruction method in Rodenburg & Bates (1992), the Wigner-distribution deconvolution (WDD) method which is still in use today for electron ptychography. Also suggested in that paper was the use of iterative methods for ptychography, examples of which were published in Faulkner & Rodenburg (2004), Rodenburg & Faulkner (2004), Maiden & Rodenburg (2009), and other studies. Another nonlinear approach to ptychographic reconstruction was proposed by D'alfonso et al. (2014).

Early experimental demonstrations of the principles of ptychography were published by Rodenburg et al. (1993), and the first experiment which imaged past the conventional TEM information limit using ptychography was published by Nellist et al. (1995). This result, shown in Figure 8d, reconstructed the structure factors for a small number of diffraction vectors, a method which requires a periodic sample. Iterative ptychography in TEM experiments that used information contained inside the STEM probe BF disk was shown by Hüe et al. (2010), and shortly thereafter Putkunz et al. (2012) demonstrated atomic-scale ptychography by imaging boron nanocones. In the same year, ptychographic reconstructions that used the electron intensity scattered beyond the probe-forming angular range were published by Humphry et al. (2012), reproduced in Figure 8e.

Using 4D-STEM experiments and a non-iterative "single-side band" reconstruction method, atomic resolution ptychography reconstructions of bilayer graphene were shown by Pennycook et al. (2015), and are plotted in Figure 8c. This work was followed by a theoretical paper by Yang et al. (2015*b*) which derived the optimum imaging conditions for focused probe ptychography and analyzed the advantages of using 4D-STEM over segmented detectors. This same group also used WDD ptychography and conventional imaging modes to analyze complex nanostructures in Yang et al. (2016*b*), shown in Figure 8f. To date, the highest resolution 4D-STEM ptychography experiments have been performed by Jiang et al. (2018). These experiments imaged bilayer MoS_2, plotted in Figure 8g. This paper estimated a resolution of 0.39 Å using an electron voltage of 80 kV, significantly beyond the conventional imaging resolution of 0.98 Å for these microscope parameters. Additionally, this paper also used simulations to determine that defocused-probe iterative ptychography outperformed both focused-probe iterative ptychography and the WDD reconstruction method by approximately a factor of 2 for signal-to-noise. Various authors have applied ptychography to solve materials science questions, including Yang et al. (2015*a*, 2017), Wang et al. (2017), dos Reis et al. (2018), Lozano et al. (2018), and Fang et al. (2019).

An interesting expansion of ptychography is the use of "hollow" diffraction patterns, whereby the 4D-STEM detector has a hole drilled in the center to allow for part or all of the unscattered electron beam to pass through into a spectrometer. Song et al. (2018) showed that even with part of the measurement signal removed, atomic-resolution phase signals can still be reconstructed. This "hollow" detector configuration is compatible with a large number of 4D-STEM techniques discussed in this paper

https://doi.org/10.1017/S1431927619000497 Published online by Cambridge University Press

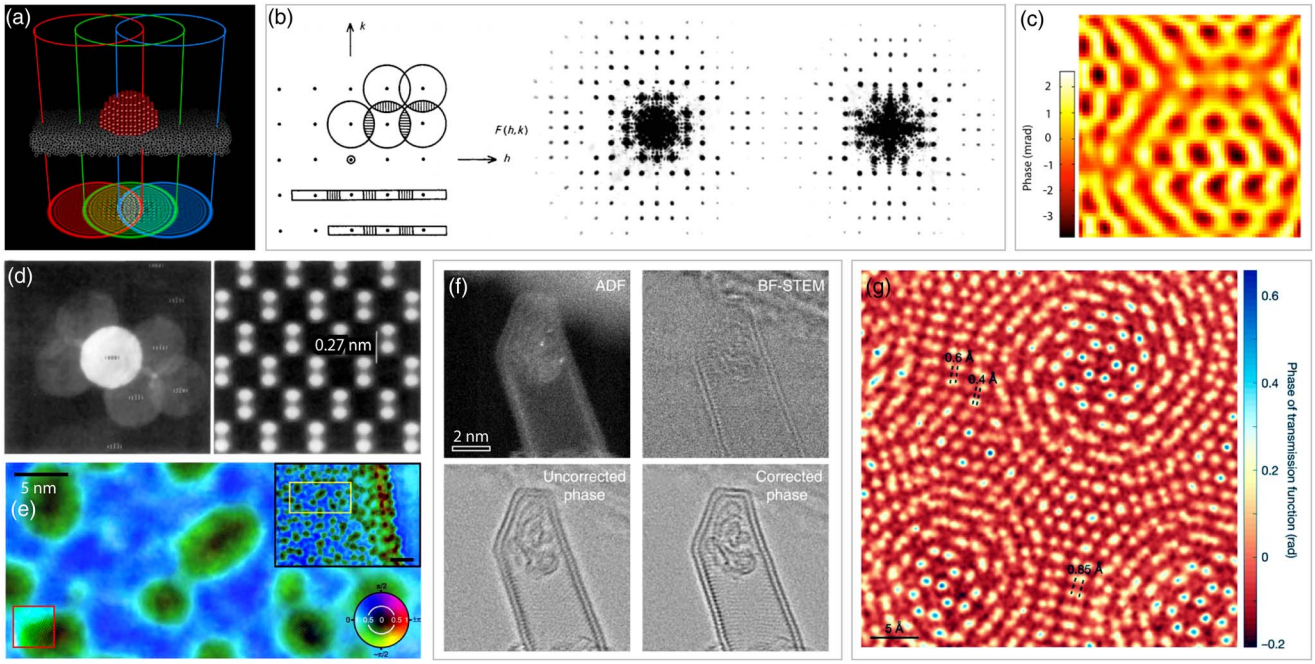

Fig. 8. Electron ptychography. **a:** Experimental geometry showing how overlapping probes (either converged or defocused) can be used to solve the exit wave phase. **b:** (Left) Schematic of convolution of square lattice with circular and rectangular probes with overlapping regions shaded, from Hoppe (1969*a*). Optical interference between diffraction of square lattice with circular hole when (center) aligned to lattice point, and (right) aligned to center of four lattice points, from Hoppe & Strube (1969). **c:** Ptychographic reconstruction of twisted bilayer graphene, from Pennycook et al. (2015). **d:** Reconstruction of periodic silicon lattice, from Nellist et al. (1995). **e:** Atomic-resolution ptychographic imaging of aperiodic samples in a modified SEM, adapted from Humphry et al. (2012), with contrast-enhanced inset. **f:** Simultaneous imaging modes including WDD ptychography of double-walled nanotube containing carbon nanostructures and iodine atoms, from Yang et al. (2016*b*). **g:** Ptychographic reconstruction of twisted bilayer MoS_2 which resolves 0.4 Å Mo dumbbells, from Jiang et al. (2018).

and we expect it to find widespread use once dedicated "hollow" pixelated STEM detectors are widely available.

Ptychography is a computational imaging method; thus in addition to benefiting from hardware such as aberration correction or better 4D-STEM detectors, algorithmic improvements are also possible. Some promising research avenues for electron ptychography have been explored in Thibault & Menzel (2013), Pelz et al. (2017), and other studies. Some authors have also explored expanding ptychography to a 3D technique by using a multislice method, including Gao et al. (2017). Others are making use of the redundancy in 4D-STEM ptychographic measurements to apply ideas from the field of compressed sensing in order to reduce the number of required measurements, such as the study by Stevens et al. (2018).

Phase Structured Electron Probes

Both DPC and ptychography rely on overlapping adjacent STEM probes to create enough redundant information for the phase of the object wave to be reconstructed. Alternatives to lateral-shift or COM DPC were also discussed in the work by Rose (1974). Rose derived that the ideal detector for measuring phase contrast from radially symmetric STEM probes is a difference signal between alternating radially symmetric "zones" aligned with the oscillations in the STEM probe's contrast transfer function, a concept further developed by Hammel & Rose (1995). The combination of defocus and spherical aberration can produce a STEM probe with a known contrast transfer function which is divided into regions of approximately 0 and $\pi/2$ rad phase shift, as shown in Figure 9c. These alternating zones are matched to multiple annular detector rings, where the probe intensity incident onto each ring is measured independently. By measuring the difference signal between the 0 and $\pi/2$ zones, the local sample phase can be measured directly with a weighted detector such as that shown in Figure 9c. This method is essentially an extension of the ABF measurement method described above (Findlay et al., 2010). However, using the probe defocus and spherical aberration limits how many difference zones can be used, and using annular ring detectors requires very precise and stable alignment of the probe with respect to the detectors.

This phase contrast measurement technique was recently updated in two ways: first by using a phase plate to produce the desired probe illumination where 50% of the probe in reciprocal space is phase shifted by $\pi/2$ rad, while the remaining regions are not phase shifted (note the shape of these zones does not matter), an experimental geometry shown in Figure 9a. Second, a pixelated electron detector is used to measure the transmitted probes in diffraction space (i.e., a 4D-STEM measurement), where a virtual detector can then be exactly matched to the phase plate pattern. This method was termed "matched illumination and detector interferometry" (MIDI)-STEM, demonstrated experimentally at atomic resolution by Ophus et al. (2016), shown in Figure 9d. MIDI-STEM produces contrast with significantly less high-pass filtering than DPC or ptychography, but is less efficient at higher spatial frequencies. Interestingly, combining MIDI-STEM with ptychography produces additional contrast making it more efficient than either method used alone (Yang et al., 2016*a*). The use of MIDI-STEM for optical sectioning was recently investigated by Lee et al. (2019), who refer to this technique (without a material phase plate) as annular differential phase contrast.

Each of the previously discussed methods for phase contrast imaging in 4D-STEM applies high-pass filtering of the phase signal of the sample to some degree. This limits the ability to use

https://doi.org/10.1017/S1431927619000497 Published online by Cambridge University Press

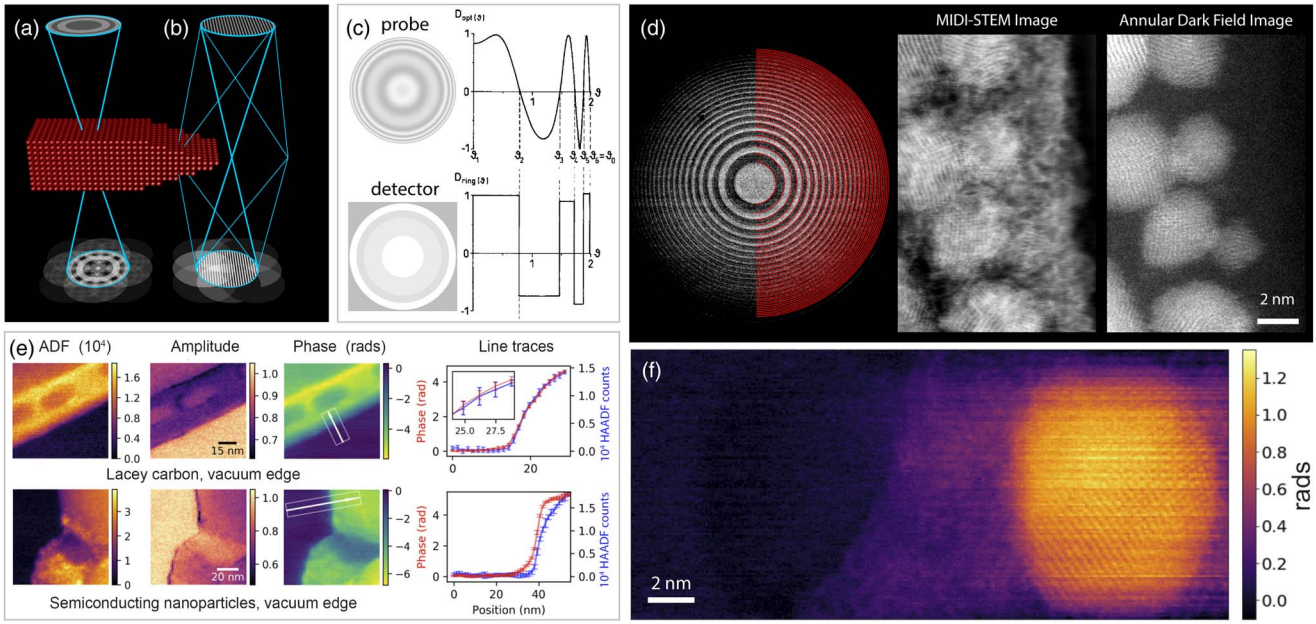

Fig. 9. 4D-STEM phase contrast measurements using structured phase probes. **a:** Schematic of MIDI-STEM and (**b**) STEMH experimental geometry. **c:** Initial MIDI-STEM proposal, adapted from Hammel & Rose (1995). **d:** MIDI-STEM experiment including phase plate image and fitted virtual detector rings, output phase contrast MIDI-STEM image, and simultaneous HAADF image, adapted from Ophus et al. (2016). **e:** Experimental demonstration of STEMH, adapted from Harvey et al. (2018). **f:** Atomic resolution STEMH phase contrast reconstruction, adapted from Yasin et al. (2018*c*).

these methods to quantitatively measure the phase shift of extended, low phase shift signals such as those induced by electric or magnetic fields (Haas et al., 2018). Recovering the low spatial frequencies can, however, be accomplished by using a reference wave, which could, for example, be generated by applying a potential to a biprism wire as in conventional electron holography (Möllenstedt & Düker, 1956). The use of a biprism wire in STEM was first discussed by Cowley (2003), but at the time detector technology was not sufficient to measure fringe shifts of a STEM-holography (STEMH) signal for many probe positions.

Another way to generate a reference wave is to use a diffraction grating in the probe-forming aperture to general multiple STEM probes, as in Figure 9b. This has been realized in 4D-STEM experiments by Harvey et al. (2018), shown in Figure 9e. By passing some of the STEM beams through vacuum and others through the sample and then measuring the fringe amplitudes and position, the absolute phase shift can be directly determined. Line traces of the experiments in Figure 9e show no phase shift in the vacuum for conductive lacey carbon, and a non-zero phase shift over vacuum outside of semiconducting nanoparticles, which was attributed to the electric field due to charging. Phase plate STEMH has also been demonstrated at atomic resolution by Yasin et al. (2018*c*), shown in Figure 9f. The STEMH method and some extensions are further discussed in Yasin et al. (2018*a*, 2018*b*).

Beyond 2D Projection and Kinematical Scattering

One of the weaknesses of electron scattering as opposed to X-ray or light scattering is that the strong interaction between electrons and matter leads to multiple scattering for all but the thinnest samples (Bethe, 1928). This "dynamical" scattering can be a problem when trying to quantitatively solve structures, but also presents an opportunity; it can be used to provide additional information about the sample along the beam direction. We previously mentioned the possible extension of ptychography to a 3D imaging method, discussed in Gao et al. (2017). This is one possible route to going beyond the 2D projection assumption, and here we briefly discuss this approach and a few others that make use of 4D-STEM experimental data. A reconstruction from Gao et al. (2017) is plotted in Figure 10a, which was calculated using the inverse multislice method for ptychography proposed by Maiden et al. (2012). A non-iterative technique to recover 3D information is the "optical sectioning" method using WDD ptychographic reconstructions at different focal planes, which was shown in Yang et al. (2016*b*).

A 4D-STEM method which solves for structure factors in the presence of dynamical scattering was shown by Wang et al. (2016). The experimental protocol used was varying the STEM probe tilt as opposed to position. By changing the relative amount of beam tilt above and below the sample (beam scan and descan respectively), this large-angle rocking-beam electron diffraction (LARBED) method developed by Koch (2011) can dramatically increase the maximum scattering angle present in each diffraction disk, relative to conventional CBED. An experimental reconstruction published by Wang et al. (2016) is shown in Figure 10b, where the large scattering vectors in LARBED allow inversion of the structure factors for $SrTiO_3$.

Another method to solve for the projected potential of thick crystals with substantial dynamical scattering is based on the idea that if the complex scattering matrix can be measured, it can be directly inverted into the structure matrix, as shown by Spence (1998) and Allen et al. (2000). This concept has been employed by Brown et al. (2018), who used a series of 4D-STEM measurements at different probe defocus values to measure the scattering matrix for crystalline silicon, plotted in Figure 10c. From this scattering matrix, they were able to directly invert the structure matrix, a result they compared with DPC measurements using both experiment and simulation.

https://doi.org/10.1017/S1431927619000497 Published online by Cambridge University Press

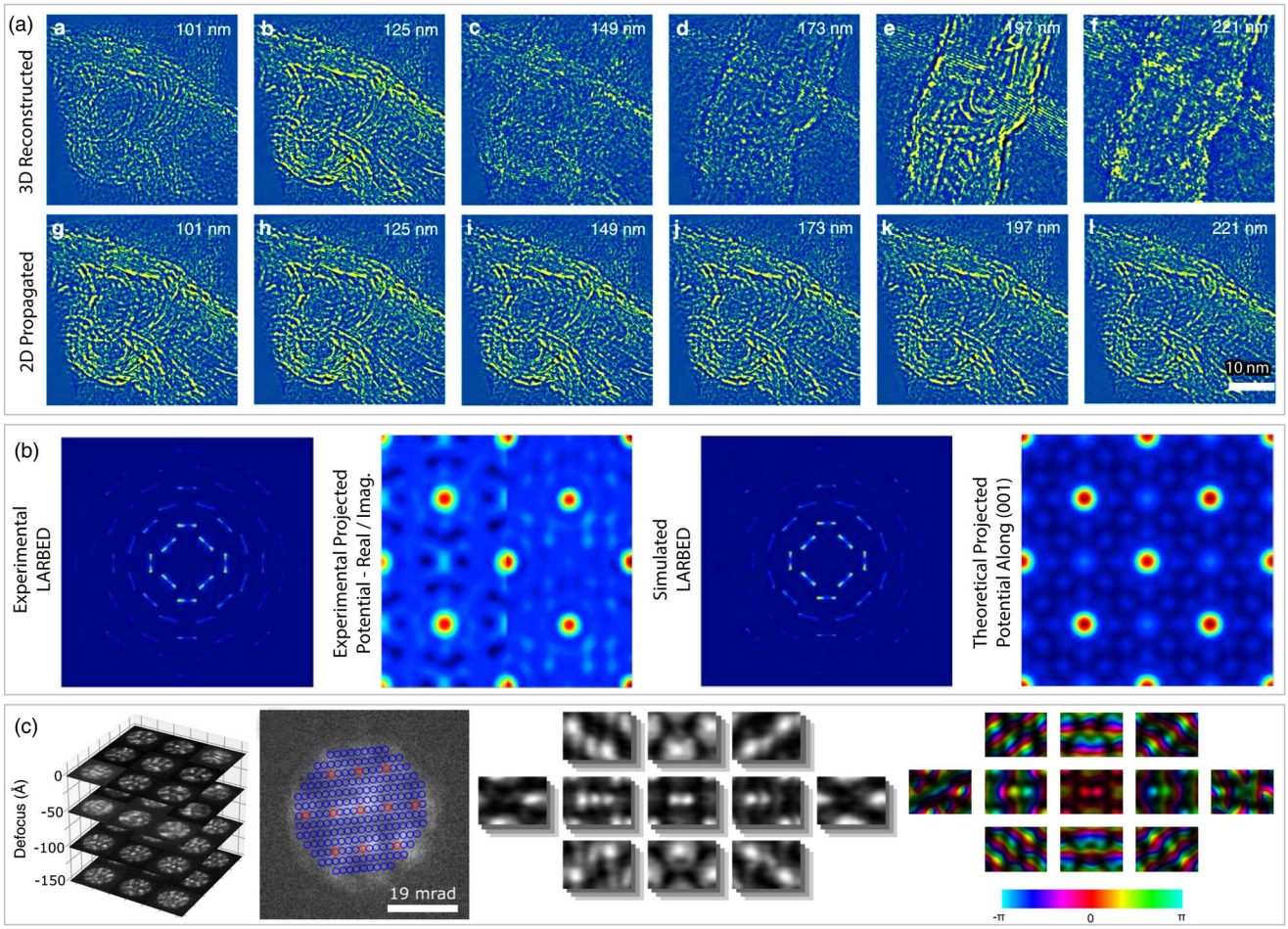

Fig. 10. 4D-STEM measurements beyond the projection assumption. **a:** Slices from 3D-ptychographic reconstruction of multiwalled carbon nanotubes, compared with Fresnel propagation of 2D reconstruction, from Gao et al. (2017). **b:** LARBED measurement and reconstructed potential of $SrTiO_3$, from Wang et al. (2016). **c:** Focal series of 4D-STEM datasets used to recover scattering matrix for (110) Si, from Brown et al. (2018).

Real-space 4D-STEM

In the final experimental section of this paper, we review some interesting experiments that further extend the capabilities of 4D-STEM by imaging the electron distribution in real space, i.e., in a plane conjugate to the sample plane as shown in Figure 11a. In this confocal configuration, apertures placed just above the detector plane can select a range of incoming ray angles, leading to enhanced depth and energy resolution. This imaging mode has long been used in optical microscopy (Webb, 1996), and was extended to electron microscopy first by Frigo et al. (2002) who dubbed the method scanning confocal electron microscopy (SCEM). Nellist et al. (2006) introduced the use of two aberration corrections in order to extend SCEM to atomic resolution, using the experimental geometry shown in Figure 11b. The first corrector is used to form an atomic-scale probe pre-specimen to remove the aberrations of the first objective lens, while the second corrector is applied post-specimen to remove the aberrations of the second objective lens. Nellist et al. (2006) were able to directly image the electron probe wavefunction at atomic resolution, improving on the resolution of previous similar measurements by Möbus & Nufer (2003).

One of the most powerful potential uses of SCEM is 3D imaging without needing to tilt the sample. Zaluzec (2007) demonstrated both improved resolution of SCEM over TEM and 3D imaging using the reduced depth of the field of SCEM. Figure 11c shows a comparison between defocused images of carbon nanocoils taken with conventional HAADF imaging compared with a SCEM measurement by Hashimoto et al. (2009). SCEM significantly improved the depth resolution, allowing Hashimoto et al. (2009) to reconstruct the 3D helical nanocoil, also plotted in Figure 11c. SCEM depth-sectioning measurements can also be performed using 4D-STEM. Hamaoka et al. (2018) demonstrated that by using an annular aperture below the specimen and recording the full diffraction pattern, 3D information from the sample could be obtained using virtual ring detectors.

By adding scanning to the experiments performed by Nellist et al. (2006) and Etheridge et al. (2011) were able to perform "4D-SCEM" experiments to directly measure the electron probe wavefunction intensity after scattering from a gold crystal. These experiments which the authors refer to as "realspace scanning transmission electron microscopy" (R-STEM) are reproduced in Figure 11d, where the electron probe was moved between two atomic columns. As the probe traverses the sample, the intensity distribution is strongly modulated by scattering from the sample, due to dynamical and channeling effects. This direct measurement of the electron distribution within the sample was previously only available via simulation. This has important ramifications for inelastic scattering measurements with electron spectroscopy,

https://doi.org/10.1017/S1431927619000497 Published online by Cambridge University Press

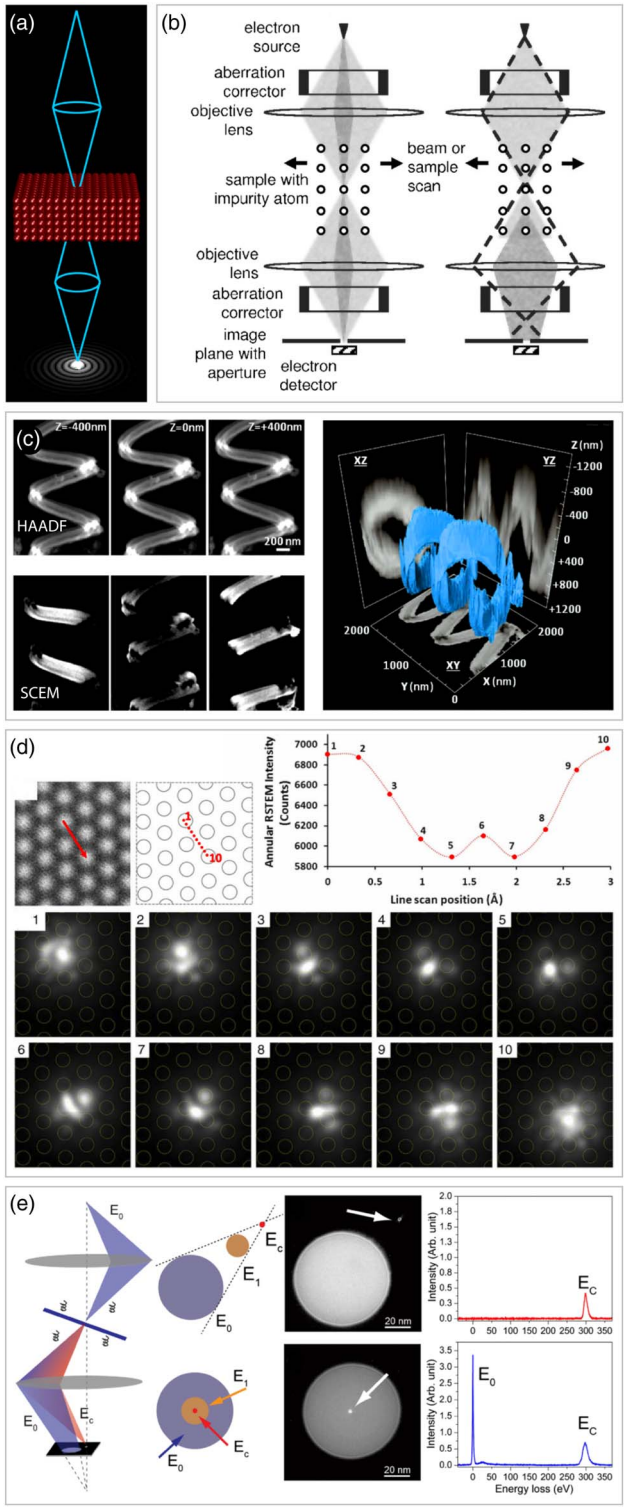

Fig. 11. R-STEM/SCEM. **a:** Schematic of imaging condition where detector plane is conjugated to the sample plane. **b:** Diagram showing how dual aberration corrections for reciprocal and real space can be used to implement SCEM, from Nellist et al. (2006). **c:** 3D reconstruction of carbon nanocoils using SCEM, adapted from Hashimoto et al. (2009). **d:** Double aberration-corrected images of electron probe in real-space after passing through crystallizing gold, from Etheridge et al. (2011). **e:** Diagram showing how off-axis SCEM can be used to measure inelastic scattering, experimental comparison of on- and off-axis SCEM imaging of carbon with 300 eV edge, compared with EELS measurements of the same edge, adapted from Zheng et al. (2014).

which the authors demonstrate with measurements of the probe after scattering from a plasmon. The same group also demonstrated direct measurements of chromatic aberration coefficients in STEM in Zheng & Etheridge (2013). Another follow-up paper by Zheng et al. (2014) introduced the concept of "off-axis" SCEM, which is shown in Figure 11e. By tilting the incident STEM probe and varying the post-scattering defocus, they use the chromatic aberration of the system in order to create a 3D dispersion which allows for spectroscopic measurements of the STEM probe without a spectrometer (i.e., without energy dispersive electron optics). Figure 11e also shows the verification of these off-axis SCEM measurements using conventional STEM-EELS spectroscopy. Further information on R-STEM experiments can be found in studies by Lazar et al. (2011) and Dwyer et al. (2012).

4D-STEM Simulation Methods

Finally, we want to briefly mention the role of simulations in 4D-STEM studies. Previously discussed examples such as Liu et al. (2013), Ophus et al. (2014), Yang et al. (2015*b*, 2017); Bruma et al. (2016), Xu & LeBeau (2018), and many others relied heavily on simulation to interpret the 4D-STEM results, not to mention the many ideas which are initially tested on, or verified by, simulations. TEM simulations are typically performed with one of two algorithms: Bloch wave scattering matrix (S-matrix) calculations (Bethe, 1928; Humphreys, 1979), or the multislice method (Cowley & Moodie, 1957; Goodman & Moodie, 1974). STEM simulations typically require significantly more calculations than plane-wave TEM calculations, since the scattering of each probe is different. In addition to this, 4D-STEM simulations require storing the full 4D output signal which could potentially require a large amount of disk storage space (Ophus et al., 2017*b*). Therefore, large 4D-STEM simulation studies usually employ the multislice method (which scales more efficiently with system size than Bloch wave methods) and utilize parallelization either over multiple central processing units, or use one or more graphics processing units. Ophus (2017) has recently developed a hybrid S-matrix and multislice simulation method that can potentially provide a large speed up for 4D-STEM simulations. Some codes that can perform 4D-STEM simulations "out of the box" include μSTEM (Forbes et al., 2010), Prismatic (Pryor et al., 2017), STEMsalabim (Oelerich et al., 2017), and Dr. Probe (Barthel, 2018).

Conclusion

This review has covered a broad cross-section of 4D-STEM experimental methods. We have chosen to focus on the wide breadth of measurements possible with 4D-STEM, as opposed to going into depth on a few topics. We hope that this review will give materials scientists ideas for new measurements they can apply to their samples using 4D-STEM, and that it provides the key references required to learn more about each of these measurement techniques. 4D-STEM methods will likely see widespread deployment, due to the current fast pace of detector hardware development, and increasing availability of analysis software. Eventually, these methods will become available and accessible enough that 4D-STEM will become just STEM.

Author ORCIDs. Colin Ophus, 0000-0003-2348-8558.

https://doi.org/10.1017/S1431927619000497 Published online by Cambridge University Press

Acknowledgments. We wish to thank Holly Barton, Thomas Pekin, Steven Zeltmann, Benjamin Savitzky, Hamish Brown, and Karen Bustillo for helpful suggestions and proof-reading of this paper. We thank Roberto dos Reis, Jim Ciston, and Peter Ercius for providing 4D-STEM datasets. We also thank Alexander Mueller for helpful translations of German manuscripts, and David Muller for suggesting the title of this manuscript. CO acknowledges support from the US Department of Energy Early Career Research Program. Work at the Molecular Foundry was supported by the Office of Science, Office of Basic Energy Sciences, the US Department of Energy under Contract No. DE-AC02-05CH11231.

References

Allen L, Faulkner H & Leeb H (2000). Inversion of dynamical electron diffraction data including absorption. *Acta Crystallogr, Sect A: Found Crystallogr* **56**(2), 119–126.

Ånes HW, Andersen IM & van Helvoort AT (2018). Crystal phase mapping by scanning precession electron diffraction and machine learning decomposition. *Microsc Microanal* **24**(S1), 586–587.

Ansari R, Beuville E, Borer K, Cenci P, Clark AG, Federspiel A, Gildemeister O, Gössling C, Hara K, Heijne EHM, Jarron P, Lariccia P, Lisowski B, Munday DJ, Pal T, Parker MA, Redaelli N, Scampoli P, Simak V, Singh SL, Vallon-Hulth T and Wells PS (1989). The silicon detectors in the UA2 experiment. *Nucl Instrum Methods Phys Res Sect A* **279**(1–2), 388–395.

Barthel J (2018). Dr. Probe: A software for high-resolution STEM image simulation. *Ultramicroscopy* **193**, 1.

Bates R & Rodenburg J (1989). Sub-Ångström transmission microscopy: A Fourier transform algorithm for microdiffraction plane intensity information. *Ultramicroscopy* **31**(3), 303–307.

Béché A, Rouviere J, Clément L & Hartmann J (2009). Improved precision in strain measurement using nanobeam electron diffraction. *Appl Phys Lett* **95** (12), 123114.

Bethe H (1928). Theorie der beugung von elektronen an kristallen. *Ann Phys* **392**(17), 55–129.

Bogle SN, Nittala LN, Twesten RD, Voyles PM & Abelson JR (2010). Size analysis of nanoscale order in amorphous materials by variable-resolution fluctuation electron microscopy. *Ultramicroscopy* **110**(10), 1273–1278.

Bozzolo N, Dewobroto N, Wenk H & Wagner F (2007). Microstructure and microtexture of highly cold-rolled commercially pure titanium. *J Mater Sci* **42**(7), 2405–2416.

Brodusch N, Demers H & Gauvin R (2013). Nanometres-resolution Kikuchi patterns from materials science specimens with transmission electron forward scatter diffraction in the scanning electron microscope. *J Microsc* **250**(1), 1–14.

Brown H, D'Alfonso A, Chen Z, Morgan A, Weyland M, Zheng C, Fuhrer M, Findlay S & Allen L (2016). Structure retrieval with fast electrons using segmented detectors. *Phys Rev B* **93**(13), 134116.

Brown HG, Chen Z, Weyland M, Ophus C, Ciston J, Allen LJ & Findlay SD (2018). Structure retrieval at atomic resolution in the presence of multiple scattering of the electron probe. *Phys Rev Lett* **121**(26), 266102.

Brown H, Ishikawa R, Shibata N, Ikuhara Y, Allen L & Findlay S (2019). Large angle illumination enabling accurate structure reconstruction from thick samples in scanning transmission electron microscopy. *Ultramicroscopy* **197**, 112–121.

Bruma A, Santiago U, Alducin D, Plascencia Villa G, Whetten RL, Ponce A, Mariscal M & José-Yacamán M (2016). Structure determination of superatom metallic clusters using rapid scanning electron diffraction. *J Phys Chem C* **120**(3), 1902–1908.

Brunetti G, Robert D, Bayle-Guillemaud P, Rouviere J, Rauch E, Martin J, Colin J, Bertin F & Cayron C (2011). Confirmation of the domino-cascade model by LiFePO/FePO precession electron diffraction. *Chem Mater* **23**(20), 4515–4524.

Bufford D, Abdeljawad F, Foiles S & Hattar K (2015). Unraveling irradiation induced grain growth with *in situ* transmission electron microscopy and coordinated modeling. *Appl Phys Lett* **107**(19), 191901.

Bustillo KC, Panova O, Chen XC, Takacs CJ, Ciston J, Ophus C, Balsara NP & Minor AM (2017). Nanobeam scanning diffraction for orientation mapping of polymers. *Microsc Microanal* **23**(S1), 1782–1783.

Caswell TA, Ercius P, Tate MW, Ercan A, Gruner SM & Muller DA (2009). A high-speed area detector for novel imaging techniques in a scanning transmission electron microscope. *Ultramicroscopy* **109**(4), 304–311.

Chapman J, McFadyen I & McVitie S (1990). Modified differential phase contrast Lorentz microscopy for improved imaging of magnetic structures. *IEEE Trans Magn* **26**(5), 1506–1511.

Chen Z, Weyland M, Ercius P, Ciston J, Zheng C, Fuhrer M, D'Alfonso A, Allen L & Findlay S (2016). Practical aspects of diffractive imaging using an atomic-scale coherent electron probe. *Ultramicroscopy* **169**, 107–121.

Clément L, Pantel R, Kwakman LT & Rouvière J (2004). Strain measurements by convergent-beam electron diffraction: The importance of stress relaxation in lamella preparations. *Appl Phys Lett* **85**(4), 651–653.

Cooper D, Denneulin T, Bernier N, Béché A & Rouvière J-L (2016). Strain mapping of semiconductor specimens with nm-scale resolution in a transmission electron microscope. *Micron* **80**, 145–165.

Cowley J (1984). The use of scanning transmission electron microscopes to study surfaces and small particles. *ACS Symp Ser* **248**, 353–366.

Cowley J (1986). Electron diffraction phenomena observed with a high resolution stem instrument. *J Electron Microsc Tech* **3**(1), 25–44.

Cowley J (1996). Electron nanodiffraction: Progress and prospects. *Microscopy* **45**(1), 3–10.

Cowley J (2003). Ultra-high resolution with off-axis STEM holography. *Ultramicroscopy* **96**(2), 163–166.

Cowley JM & Moodie AF (1957). The scattering of electrons by atoms and crystals. I. a new theoretical approach. *Acta Crystallogr* **10**(10), 609–619.

Cowley J & Ou H-J (1989). Observation of microdiffraction patterns with a dedicated STEM instrument. *J Electron Microsc Tech* **11**(2), 143–154.

Cowley J & Spence JC (1979). Innovative imaging and microdiffraction in stem. *Ultramicroscopy* **2**(9), 433–438.

D'alfonso A, Morgan A, Yan A, Wang P, Sawada H, Kirkland A & Allen L (2014). Deterministic electron ptychography at atomic resolution. *Phys Rev B* **89**(6), 064101.

Darbal A, Gemmi M, Portillo J, Rauch E & Nicolopoulos S (2012). Nanoscale automated phase and orientation mapping in the TEM. *Micros Today* **20**(6), 38–42.

Dekkers N & De Lang H (1974). Differential phase contrast in a STEM. *Optik* **41**(4), 452–456.

De Ruijter W (1995). Imaging properties and applications of slow-scan charge-coupled device cameras suitable for electron microscopy. *Micron* **26**(3), 247–275.

Dey S, Morawiec A, Bouzy E, Hazotte A & Fundenberger J-J (2006). A technique for determination of γ/γ interface relationships in a $(\alpha 2 + \gamma)$ TiAl base alloy using TEM Kikuchi patterns. *Mater Lett* **60**(5), 646–650.

Dierickx B, Meynants G & Scheffer D (1997). Near-100% fill factor standard CMOS active pixel. *Proceedings 1997 CCD & AIS Workshop P*, 1.

dos Reis R, Yang H, Ophus C, Ercius P, Bizarri G, Perrodin D, Shalapska T, Bourret E, Ciston J & Dahmen U (2018). Determination of the structural phase and octahedral rotation angle in halide perovskites. *Appl Phys Lett* **112**(7), 071901.

Dwyer C, Lazar S, Chang L & Etheridge J (2012). Image formation in the scanning transmission electron microscope using object-conjugate detectors. *Acta Crystallogr, Sect A* **68**(2), 196–207.

Ebner C, Sarkar R, Rajagopalan J & Rentenberger C (2016). Local, atomic-level elastic strain measurements of metallic glass thin films by electron diffraction. *Ultramicroscopy* **165**, 51–58.

Egerton R (2019). Radiation damage to organic and inorganic specimens in the TEM. *Micron* **119**, 72–87.

Eggeman AS, Krakow R & Midgley PA (2015). Scanning precession electron tomography for three-dimensional nanoscale orientation imaging and crystallographic analysis. *Nat Commun* **6**, 7267.

Ercan A, Tate M & Gruner S (2006). Analog pixel array detectors. *J Synchrotron Radiat* **13**(2), 110–119.

Etheridge J, Lazar S, Dwyer C & Botton GA (2011). Imaging high-energy electrons propagating in a crystal. *Phys Rev Lett* **106**(16), 160802.

Fan G & Ellisman MH (1993). High-sensitivity lens-coupled slow-scan CCD camera for transmission electron microscopy. *Ultramicroscopy* **52**(1), 21–29.

Fang S, Wen Y, Allen C, Ophus C, Han G, Kirkland A, Kaxiras E & Warner J (2019). Atomic electrostatic maps of 1D channels in 2D

https://doi.org/10.1017/S1431927619000497 Published online by Cambridge University Press

semiconductors using 4D scanning transmission electron microscopy. *Nat Commun* **10**, 1127.

Fatermans J, den Dekker A, Müller-Caspary K, Lobato I, OLeary C, Nellist P & Van Aert S (2018). Single atom detection from low contrast-to-noise ratio electron microscopy images. *Phys Rev Lett* **121**(5), 056101.

Faulkner H & Rodenburg J (2004). Movable aperture lensless transmission microscopy: A novel phase retrieval algorithm. *Phys Rev Lett* **93**(2), 023903.

Favia P, Popovici M, Eneman G, Wang G, Bargallo-Gonzalez M, Simoen E, Menou N & Bender H (2010). Nano-beam diffraction: Crystal structure and strain analysis at the nanoscale. *ECS Trans* **33**(11), 205–219.

Favia P, Gonzales MB, Simoen E, Verheyen P, Klenov D & Bender H (2011). Nanobeam diffraction: Technique evaluation and strain measurement on complementary metal oxide semiconductor devices. *J Electrochem Soc* **158**(4), H438–H446.

Findlay S, Shibata N, Sawada H, Okunishi E, Kondo Y & Ikuhara Y (2010). Dynamics of annular bright field imaging in scanning transmission electron microscopy. *Ultramicroscopy* **110**(7), 903–923.

Florea I, Ersen O, Arenal R, Ihiawakrim D, Messaoudi C, Chizari K, Janowska I & Pham-Huu C (2012). 3D analysis of the morphology and spatial distribution of nitrogen in nitrogen-doped carbon nanotubes by energy-filtered transmission electron microscopy tomography. *J Am Chem Soc* **134**(23), 9672–9680.

Forbes B, Martin A, Findlay S, DAlfonso A & Allen L (2010). Quantum mechanical model for phonon excitation in electron diffraction and imaging using a Born-Oppenheimer approximation. *Phys Rev B* **82**(10), 104103.

Françon M (1954). *Le Microscope à Contraste de Phase et le Microscope Interférentiel*, vol. 1. Paris, France: Centre National de la Recherche Scientifique.

Frigo SP, Levine ZH & Zaluzec NJ (2002). Submicron imaging of buried integrated circuit structures using scanning confocal electron microscopy. *Appl Phys Lett* **81**(11), 2112–2114.

Fundenberger J-J, Morawiec A, Bouzy E & Lecomte J-S (2003). Polycrystal orientation maps from TEM. *Ultramicroscopy* **96**(2), 127–137.

Gallagher-Jones M, Ophus C, Bustillo KC, Boyer DR, Panova O, Glynn C, Zee C-T, Ciston J, Mancia KC, Minor AM & Rodriguez JA (2019). Nanoscale mosaicity revealed in peptide microcrystals by scanning electron nanodiffraction. *Commun Biol* **2**, 26.

Gammer C, Ozdol VB, Liebscher CH & Minor AM (2015). Diffraction contrast imaging using virtual apertures. *Ultramicroscopy* **155**, 1–10.

Gammer C, Ophus C, Pekin TC, Eckert J & Minor AM (2018). Local nanoscale strain mapping of a metallic glass during *in situ* testing. *Appl Phys Lett* **112**(17), 171905.

Gao S, Wang P, Zhang F, Martinez GT, Nellist PD, Pan X & Kirkland AI (2017). Electron ptychographic microscopy for three-dimensional imaging. *Nat Commun* **8**(1), 163.

Garner A, Gholinia A, Frankel P, Gass M, MacLaren I & Preuss M (2014). The microstructure and microtexture of zirconium oxide films studied by transmission electron backscatter diffraction and automated crystal orientation mapping with transmission electron microscopy. *Acta Mater* **80**, 159–171.

Goodman P & Moodie A (1974). Numerical evaluations of N-beam wave functions in electron scattering by the multi-slice method. *Acta Crystallogr, Sect A: Cryst Phys, Diffr, Theor Gen Crystallogr* **30**(2), 280–290.

Goris B, Turner S, Bals S & Van Tendeloo G (2014). Three-dimensional valency mapping in ceria nanocrystals. *ACS Nano* **8**(10), 10878–10884.

Grieb T, Krause FF, Mahr C, Zillmann D, Müller-Caspary K, Schowalter M & Rosenauer A (2017). Optimization of NBED simulations for disc-detection measurements. *Ultramicroscopy* **181**, 50–60.

Grieb T, Krause FF, Schowalter M, Zillmann D, Sellin R, Müller-Caspary K, Mahr C, Mehrtens T, Bimberg D & Rosenauer A (2018). Strain analysis from nano-beam electron diffraction: Influence of specimen tilt and beam convergence. *Ultramicroscopy* **190**, 45–57.

Grimley ED, Schenk T, Mikolajick T, Schroeder U & LeBeau JM (2018). Atomic structure of domain and interphase boundaries in ferroelectric HfO. *Adv Mater Interfaces* **5**(5), 1701258.

Guo Q & Thompson GB (2018). In-situ indentation and correlated precession electron diffraction analysis of a polycrystalline Cu thin film. *JOM* **70**(7), 1–7.

Guzzinati G, Ghielens W, Mahr C, Béché A, Rosenauer A, Calders T & Verbeeck J (2019). Electron bessel beam diffraction for precise and accurate nanoscale strain mapping. *arXiv preprint arXiv*:1902.06979.

Haas B, Thomas C, Jouneau P-H, Bernier N, Meunier T, Ballet P & Rouvière J-L (2017). High precision strain mapping of topological insulator HgTe/CdTe. *Appl Phys Lett* **110**(26), 263102.

Haas B, Rouvière J-L, Boureau V, Berthier R & Cooper D (2018). Direct comparison of off-axis holography and differential phase contrast for the mapping of electric fields in semiconductors by transmission electron microscopy. *Ultramicroscopy* **198**, 58–72.

Hachtel JA, Idrobo JC & Chi M (2018). Sub-Ångstrom electric field measurements on a universal detector in a scanning transmission electron microscope. *Adv Struct Chemi Imaging* **4**(1), 10.

Haider M, Epstein A, Jarron P & Boulin C (1994). A versatile, software configurable multichannel STEM detector for angle-resolved imaging. *Ultramicroscopy* **54**(1), 41–59.

Hamaoka T, Hashimoto A, Mitsuishi K & Takeguchi M (2018). 4D-data acquisition in scanning confocal electron microscopy for depth-sectioned imaging. *e-J Surf Sci Nanotechnol* **16**, 247–252.

Hammel M & Rose H (1995). Optimum rotationally symmetric detector configurations for phase-contrast imaging in scanning transmission electron microscopy. *Ultramicroscopy* **58**(3–4), 403–415.

Han Y, Nguyen K, Cao M, Cueva P, Xie S, Tate M, Purohit P, Gruner S, Park J & Muller D (2018). Strain mapping of two-dimensional heterostructures with subpicometer precision. *Nano Lett* **18**(6), 3746.

Harvey TR, Yasin FS, Chess JJ, Pierce JS, dos Reis RMS, Özdöl VB, Ercius P, Ciston J, Feng W, Kotov NA, McMorran BJ & Ophus C (2018). Interpretable and efficient interferometric contrast in scanning transmission electron microscopy with a diffraction-grating beam splitter. *Phys Rev Appl* **10**, 061001.

Hashimoto A, Shimojo M, Mitsuishi K & Takeguchi M (2009). Three-dimensional imaging of carbon nanostructures by scanning confocal electron microscopy. *J Appl Phys* **106**(8), 086101.

Hawkes P (1982). Is the STEM a ptychograph? *Ultramicroscopy* **9**(1–2), 27–30.

Hegerl R & Hoppe W (1970). Dynamische theorie der kristallstrukturanalyse durch elektronenbeugung im inhomogenen primärstrahlwellenfeld. *Berichte der Bunsengesellschaft für Physikalische Chemie* **74**(11), 1148–1154.

Hilke S, Kirschbaum J, Hieronymus-Schmidt V, Radek M, Bracht H, Wilde G & Peterlechner M (2019). Analysis of medium-range order based on simulated segmented ring detector STEM-images: Amorphous Si. *Ultramicroscopy* **200**, 169–179.

Hirata A, Guan P, Fujita T, Hirotsu Y, Inoue A, Yavari AR, Sakurai T & Chen M (2011). Direct observation of local atomic order in a metallic glass. *Nat Mater* **10**(1), 28.

Hoppe W (1969*a*). Beugung im inhomogenen primärstrahlwellenfeld. I. prinzip einer phasenmessung von elektronenbeungungsinterferenzen. *Acta Crystallogr, Sect A: Cryst Phys, Diffr, Theor Gen Crystallogr* **25**(4), 495–501.

Hoppe W (1969*b*). Beugung im inhomogenen primärstrahlwellenfeld. III. amplituden-und phasenbestimmung bei unperiodischen objekten. *Acta Crystallogr, Sect A: Cryst Phys, Diffr, Theor Gen Crystallogr* **25**(4), 508–514.

Hoppe W & Strube G (1969). Beugung in inhomogenen primärstrahlenwellenfeld. II. lichtoptische analogieversuche zur phasenmessung von gitterinterferenzen. *Acta Crystallogr, Sect A: Cryst Phys, Diffr, Theor Gen Crystallogr* **25**(4), 502–507.

Hou J, Ashling CW, Collins SM, Krajnc A, Zhou C, Longley L, Johnstone D, Chater PA, Li S, Coudert F-X, Keen DA, Midgley PA, Mali G, Chen V & Bennett T (2018). Metal-organic framework crystal-glass composites. *ChemRxiv*, 7093862v1.

Hüe F, Rodenburg J, Maiden A, Sweeney F & Midgley P (2010). Wave-front phase retrieval in transmission electron microscopy via ptychography. *Phys Rev B* **82**(12), 121415.

Humphreys C (1979). The scattering of fast electrons by crystals. *Rep Prog Phys* **42**(11), 1825.

Humphry M, Kraus B, Hurst A, Maiden A & Rodenburg J (2012). Ptychographic electron microscopy using high-angle dark-field scattering for sub-nanometre resolution imaging. *Nat Commun* **3**, 730.

Hwang J, Melgarejo Z, Kalay Y, Kalay I, Kramer MJ, Stone D & Voyles P (2012). Nanoscale structure and structural relaxation in $Zr_{50}Cu_{45}Al_5$ bulk metallic glass. *Phys Rev Lett* **108**(19), 195505.

Hwang J, Zhang JY, DAlfonso AJ, Allen LJ & Stemmer S (2013). Three-dimensional imaging of individual dopant atoms in $SrTiO_3$. *Phys Rev Lett* **111**(26), 266101.

https://doi.org/10.1017/S1431927619000497 Published online by Cambridge University Press

Hÿtch MJ & Minor AM (2014). Observing and measuring strain in nanostructures and devices with transmission electron microscopy. *MRS Bull* **39**(2), 138–146.

Idrissi H, Kobler A, Amin-Ahmadi B, Coulombier M, Galceran M, Raskin J-P, Godet S, Kübel C, Pardoen T & Schryvers D (2014). Plasticity mechanisms in ultrafine grained freestanding aluminum thin films revealed by in-situ transmission electron microscopy nanomechanical testing. *Appl Phys Lett* **104**(10), 101903.

Im S, Chen Z, Johnson JM, Zhao P, Yoo GH, Park ES, Wang Y, Muller DA & Hwang J (2018). Direct determination of structural heterogeneity in metallic glasses using four-dimensional scanning transmission electron microscopy. *Ultramicroscopy* **195**, 189–193.

Izadi E, Darbal A, Sarkar R & Rajagopalan J (2017). Grain rotations in ultrafine-grained aluminum films studied using *in situ* tem straining with automated crystal orientation mapping. *Mater Des* **113**, 186–194.

Jarausch K, Thomas P, Leonard DN, Twesten R & Booth CR (2009). Four-dimensional STEM-EELS: Enabling nano-scale chemical tomography. *Ultramicroscopy* **109**(4), 326–337.

Jiang Y, Chen Z, Han Y, Deb P, Gao H, Xie S, Purohit P, Tate MW, Park J, Gruner SM *et al.* (2018). Electron ptychography of 2D materials to deep sub-Ångström resolution. *Nature* **559**(7714), 343.

Johnson IJ, Bustillo KC, Ciston J, Draney BR, Ercius P, Fong E, Goldschmidt A, Joseph JM, Lee JR, Minor AM, *et al.* (2018). A next generation electron microscopy detector aimed at enabling new scanning diffraction techniques and online data reconstruction. *Microsc Microanal* **24** (S1), 166–167.

Jones L & Nellist PD (2013). Advances in 2D, 3D and 4D STEM image data analysis. *Microsc Microanal* **19**(S2), 770–771.

Jones P, Rackham G & Steeds JW (1977). Higher order Laue zone effects in electron diffraction and their use in lattice parameter determination. *Proc R Soc London, Ser A* **354**(1677), 197–222.

Kaufman M, Pearson D & Fraser H (1986). The use of convergent-beam electron diffraction to determine local lattice distortions in nickel-base superalloys. *Philos Mag A* **54**(1), 79–92.

Kikuchi S (1928). Elektronenbeugung an glimmerplättchen. *Jpn J Phys* **5**, 23.

Kimoto K & Ishizuka K (2011). Spatially resolved diffractometry with atomic-column resolution. *Ultramicroscopy* **111**(8), 1111–1116.

Kobler A, Kashiwar A, Hahn H & Kübel C (2013). Combination of *in situ* straining and ACOM TEM: A novel method for analysis of plastic deformation of nanocrystalline metals. *Ultramicroscopy* **128**, 68–81.

Koch CT (2011). Aberration-compensated large-angle rocking-beam electron diffraction. *Ultramicroscopy* **111**(7), 828–840.

Koch CT, Özdöl VB & Ishizuka K (2012). Quantitative four-dimensional electron diffraction in the TEM. *Microsc Anal* **26**(4), 5–8.

Konnert J & D'Antonio P (1986). Image reconstruction using electron microdiffraction patterns from overlapping regions. *Ultramicroscopy* **19**(3), 267–277.

Krajnak M, McGrouther D, Maneuski D, O'Shea V & McVitie S (2016). Pixelated detectors and improved efficiency for magnetic imaging in STEM differential phase contrast. *Ultramicroscopy* **165**, 42–50.

Lazar S, Etheridge J, Dwyer C, Freitag B & Botton GA (2011). Atomic resolution imaging using the real-space distribution of electrons scattered by a crystalline material. *Acta Crystallogr, Sect A: Found Crystallogr* **67**(5), 487–490.

Lazić I, Bosch EG & Lazar S (2016). Phase contrast STEM for thin samples: Integrated differential phase contrast. *Ultramicroscopy* **160**, 265–280.

LeBeau JM, Findlay SD, Wang X, Jacobson AJ, Allen LJ & Stemmer S (2009). High-angle scattering of fast electrons from crystals containing heavy elements: Simulation and experiment. *Phys Rev B* **79**(21), 214110.

LeBeau JM, Findlay SD, Allen LJ & Stemmer S (2010). Position averaged convergent beam electron diffraction: Theory and applications. *Ultramicroscopy* **110**(2), 118–125.

Lee Z, Kaiser U & Rose H (2019). Prospects of annular differential phase contrast applied for optical sectioning in STEM. *Ultramicroscopy* **196**, 58–66.

Li X, Mooney P, Zheng S, Booth CR, Braunfeld MB, Gubbens S, Agard DA & Cheng Y (2013). Electron counting and beam-induced motion correction enable near-atomic-resolution single-particle cryo-EM. *Nat Methods* **10**(6), 584.

Li X, Dyck OE, Oxley MP, Lupini AR, McInnes L, Healy J, Jesse S & Kalinin SV (2019). Manifold learning of four-dimensional scanning transmission electron microscopy. *NPJ Comput Mater* **5**(1), 5.

Liu J, Li K, Pandey S, Benistant F, See A, Zhou M, Hsia L, Schampers R & Klenov DO (2008). Strain relaxation in transistor channels with embedded epitaxial silicon germanium source/drain. *Appl Phys Lett* **93**(22), 221912.

Liu A, Neish M, Stokol G, Buckley G, Smillie L, de Jonge M, Ott R, Kramer M & Bourgeois L (2013). Systematic mapping of icosahedral short-range order in a melt-spun ZrCu metallic glass. *Phys Rev Lett* **110**(20), 205505.

Liu AC, Lumpkin GR, Petersen TC, Etheridge J & Bourgeois L (2015). Interpretation of angular symmetries in electron nanodiffraction patterns from thin amorphous specimens. *Acta Crystallogr, Sect A: Found Adv* **71**(5), 473–482.

Lozano JG, Martinez GT, Jin L, Nellist PD & Bruce PG (2018). Low-dose aberration-free imaging of Li-rich cathode materials at various states of charge using electron ptychography. *Nano Lett* **18**(11), 6850–6855.

Lubk A & Zweck J (2015). Differential phase contrast: An integral perspective. *Phys Rev A* **91**(2), 023805.

Lupini AR, Chi M, Kalinin SV, Borisevich AY, Idrobo JC & Jesse S (2015). Ptychographic imaging in an aberration corrected stem. *Microsc Microanal* **21**(S3), 1219–1220.

MacArthur K, Pennycook T, Okunishi E, D'Alfonso A, Lugg N, Allen L, Nellist P, *et al.* (2013). Probe integrated scattering cross sections in the analysis of atomic resolution HAADF STEM images. *Ultramicroscopy* **133**, 109–119.

MacLaren I, Villaurrutia R & Peláiz-Barranco A (2010). Domain structures and nanostructures in incommensurate antiferroelectric $Pb_xLa_{1-x}(Zr_{0.9-}Ti_{0.1})O_3$. *J Appl Phys* **108**(3), 034109.

Mahr C, Müller-Caspary K, Grieb T, Schowalter M, Mehrtens T, Krause FF, Zillmann D & Rosenauer A (2015). Theoretical study of precision and accuracy of strain analysis by nano-beam electron diffraction. *Ultramicroscopy* **158**, 38–48.

Mahr C, Müller-Caspary K, Ritz R, Simson M, Grieb T, Schowalter M, Krause FF, Lackmann A, Soltau H, Wittstock A, *et al.* (2019). Influence of distortions of recorded diffraction patterns on strain analysis by nano-beam electron diffraction. *Ultramicroscopy* **196**, 74–82.

Maiden AM & Rodenburg JM (2009). An improved ptychographical phase retrieval algorithm for diffractive imaging. *Ultramicroscopy* **109** (10), 1256–1262.

Maiden AM, Humphry MJ & Rodenburg J (2012). Ptychographic transmission microscopy in three dimensions using a multi-slice approach. *JOSA A* **29**(8), 1606–1614.

McMullan G, Faruqi A, Clare D & Henderson R (2014). Comparison of optimal performance at 300 keV of three direct electron detectors for use in low dose electron microscopy. *Ultramicroscopy* **147**, 156–163.

Mendis SK, Kemeny SE, Gee RC, Pain B, Staller CO, Kim Q & Fossum ER (1997). CMOS active pixel image sensors for highly integrated imaging systems. *IEEE J Solid-State Circuits* **32**(2), 187–197.

Midgley PA & Eggeman AS (2015). Precession electron diffraction–a topical review. *IUCrJ* **2**(1), 126–136.

Midgley PA & Thomas JM (2014). Multi-dimensional electron microscopy. *Angew Chem, Int Ed* **53**(33), 8614–8617.

Milazzo A-C, Leblanc P, Duttweiler F, Jin L, Bouwer JC, Peltier S, Ellisman M, Bieser F, Matis HS, Wieman H, *et al.* (2005). Active pixel sensor array as a detector for electron microscopy. *Ultramicroscopy* **104** (2), 152–159.

Möbus G & Nufer S (2003). Nanobeam propagation and imaging in a FEGTEM/STEM. *Ultramicroscopy* **96**(3–4), 285–298.

Mohammadi E, Zhao C, Meng Y, Qu G, Zhang F, Zhao X, Mei J, Zuo J-M, Shukla D & Diao Y (2017). Dynamic-template-directed multiscale assembly for large-area coating of highly-aligned conjugated polymer thin films. *Nat Commun* **8**, 16070.

Möllenstedt G & Düker H (1956). Beobachtungen und messungen an biprisma-interferenzen mit elektronenwellen. *Z Phys* **145**(3), 377–397.

Morawiec A, Bouzy E, Paul H & Fundenberger J-J (2014). Orientation precision of TEM-based orientation mapping techniques. *Ultramicroscopy* **136**, 107–118.

Müller K, Rosenauer A, Schowalter M, Zweck J, Fritz R & Volz K (2012*a*). Strain measurement in semiconductor heterostructures by scanning transmission electron microscopy. *Microsc Microanal* **18**(5), 995–1009.

https://doi.org/10.1017/S1431927619000497 Published online by Cambridge University Press

Müller K, Ryll H, Ordavo I, Ihle S, Strüder L, Volz K, Zweck J, Soltau H & Rosenauer A (2012*b*). Scanning transmission electron microscopy strain measurement from millisecond frames of a direct electron charge coupled device. *Appl Phys Lett* **101**(21), 212110.

Müller K, Krause FF, Béché A, Schowalter M, Galioit V, Löffler S, Verbeeck J, Zweck J, Schattschneider P & Rosenauer A (2014). Atomic electric fields revealed by a quantum mechanical approach to electron picodiffraction. *Nat Commun* **5**, 5653.

Müller-Caspary K, Oelsner A & Potapov P (2015). Two-dimensional strain mapping in semiconductors by nano-beam electron diffraction employing a delay-line detector. *Appl Phys Lett* **107**(7), 072110.

Müller-Caspary K, Krause FF, Grieb T, Löffler S, Schowalter M, Béché A, Galioit V, Marquardt D, Zweck J, Schattschneider P, *et al.* (2017). Measurement of atomic electric fields and charge densities from average momentum transfers using scanning transmission electron microscopy. *Ultramicroscopy* **178**, 62–80.

Müller-Caspary K, Duchamp M, Rösner M, Migunov V, Winkler F, Yang H, Huth M, Ritz R, Simson M, Ihle S, *et al.* (2018*a*). Atomic-scale quantification of charge densities in two-dimensional materials. *Phys Rev B* **98**(12), 121408.

Müller-Caspary K, Krause FF, Winkler F, Béché A, Verbeeck J, VanAert S & Rosenauer A (2018*b*). Comparison of first moment STEM with conventional differential phase contrast and the dependence on electron dose. *Ultramicroscopy* **203**, 95–104.

Nellist P, McCallum B & Rodenburg JM (1995). Resolution beyond the "information limit" in transmission electron microscopy. *Nature* **374**(6523), 630.

Nellist P, Behan G, Kirkland A & Hetherington C (2006). Confocal operation of a transmission electron microscope with two aberration correctors. *Appl Phys Lett* **89**(12), 124105.

Nord M, Krajnak M, Bali R, Hlawacek G, Liersch V, Fassbender J, McVitie S, Paterson GW, Maclaren I & McGrouther D (2016). Developing rapid and advanced visualisation of magnetic structures using 2-D pixelated STEM detectors. *Microsc Microanal* **22**(S3), 530–531.

Nord M, Ross A, McGrouther D, Barthel J, Moreau M, Hallsteinsen I, Tybell T & MacLaren I (2018). 3D sub-nanoscale imaging of unit cell doubling due to octahedral tilting and cation modulation in strained perovskite thin films. *arXiv preprint arXiv:*1810.07501.

Oelerich JO, Duschek L, Belz J, Beyer A, Baranovskii SD & Volz K (2017). STEMsalabim: A high-performance computing cluster friendly code for scanning transmission electron microscopy image simulations of thin specimens. *Ultramicroscopy* **177**, 91–96.

Ophus C (2017). A fast image simulation algorithm for scanning transmission electron microscopy. *Adv Struct Chem Imaging* **3**(1), 13.

Ophus C, Ercius P, Sarahan M, Czarnik C & Ciston J (2014). Recording and using 4D-STEM datasets in materials science. *Microsc Microanal* **20**(S3), 62–63.

Ophus C, Ciston J, Pierce J, Harvey TR, Chess J, McMorran BJ, Czarnik C, Rose HH & Ercius P (2016). Efficient linear phase contrast in scanning transmission electron microscopy with matched illumination and detector interferometry. *Nat Commun* **7**, 10719.

Ophus C, Ercius P, Huijben M & Ciston J (2017*a*). Non-spectroscopic composition measurements of $SrTiO\text{-}LaSr_{0.3}MnO$ multilayers using scanning convergent beam electron diffraction. *Appl Phys Lett* **110**(6), 063102.

Ophus C, Yang H, dos Reis R, Meng Y, Pryor A, Miao J, Pekin TC, Minor AM, Johnson I, Denes P, *et al.* (2017*b*). Computational methods for large scale scanning transmission electron microscopy (STEM) experiments and simulations. *Microsc Microanal* **23**(S1), 162–163.

Ozdol V, Gammer C, Jin X, Ercius P, Ophus C, Ciston J & Minor A (2015). Strain mapping at nanometer resolution using advanced nano-beam electron diffraction. *Appl Phys Lett* **106**(25), 253107.

Panova O, Chen XC, Bustillo KC, Ophus C, Bhatt MP, Balsara N & Minor AM (2016). Orientation mapping of semicrystalline polymers using scanning electron nanobeam diffraction. *Micron* **88**, 30–36.

Pekin TC, Gammer C, Ciston J, Minor AM & Ophus C (2017). Optimizing disk registration algorithms for nanobeam electron diffraction strain mapping. *Ultramicroscopy* **176**, 170–176.

Pekin TC, Gammer C, Ciston J, Ophus C & Minor AM (2018). *In situ* nanobeam electron diffraction strain mapping of planar slip in stainless steel. *Scr Mater* **146**, 87–90.

Pelz PM, Qiu WX, Bücker R, Kassier G & Miller RD (2017). Low-dose cryo electron ptychography via non-convex Bayesian optimization. *Sci Rep* **7**(1), 9883.

Pennycook SJ & Nellist PD (2011). *Scanning Transmission Electron Microscopy*. New York, USA: Springer-Verlag.

Pennycook TJ, Lupini AR, Yang H, Murfitt MF, Jones L & Nellist PD (2015). Efficient phase contrast imaging in stem using a pixelated detector. Part 1: Experimental demonstration at atomic resolution. *Ultramicroscopy* **151**, 160–167.

Phillips JC (1979). Topology of covalent non-crystalline solids I: Short-range order in chalcogenide alloys. *J Non-Cryst Solids* **34**(2), 153–181.

Pryor A, Ophus C & Miao J (2017). A streaming multi-GPU implementation of image simulation algorithms for scanning transmission electron microscopy. *Adv Struct Chem Imaging* **3**(1), 15.

Putkunz CT, DAlfonso AJ, Morgan AJ, Weyland M, Dwyer C, Bourgeois L, Etheridge J, Roberts A, Scholten RE, Nugent KA, *et al.* (2012). Atom-scale ptychographic electron diffractive imaging of boron nitride cones. *Phys Rev Lett* **108**(7), 073901.

Rauch E & Dupuy L (2005). Rapid spot diffraction patterns identification through template matching. *Arch Metall Mater* **50**, 87–99.

Rauch E & Véron M (2014). Automated crystal orientation and phase mapping in TEM. *Mater Charact* **98**, 1–9.

Rauch EF, Portillo J, Nicolopoulos S, Bultreys D, Rouvimov S & Moeck P (2010). Automated nanocrystal orientation and phase mapping in the transmission electron microscope on the basis of precession electron diffraction. *Z Kristallogr* **225**(2–3), 103–109.

Reisinger M, Zalesak J, Daniel R, Tomberger M, Weiss J, Darbal A, Petrenec M, Zechner J, Daumiller I, Ecker W, Sartory B & Keckes J (2016). Cross-sectional stress distribution in AlGaN heterostructure on Si (111) substrate characterized by ion beam layer removal method and precession electron diffraction. *Mater Des* **106**, 476–481.

Rodenburg J (1999). Measurement of higher-order correlation functions in amorphous materials via coherent microdiffraction. Electron Microscopy and Analysis 1999: Proceedings of the Institute of Physics Electron Microscopy and Analysis Group Conference, University of Sheffield, 24–27 August 1999, 161:145.

Rodenburg J & Bates R (1992). The theory of super-resolution electron microscopy via Wigner-distribution deconvolution. *Phil Trans R Soc London, Ser A* **339**(1655), 521–553.

Rodenburg JM & Faulkner HM (2004). A phase retrieval algorithm for shifting illumination. *Appl Phys Lett* **85**(20), 4795–4797.

Rodenburg J, McCallum B & Nellist P (1993). Experimental tests on double-resolution coherent imaging via STEM. *Ultramicroscopy* **48**(3), 304–314.

Ronchi V (1964). Forty years of history of a grating interferometer. *Appl Opt* **3**(4), 437–451.

Rose H (1974). Phase contrast in scanning transmission electron microscopy. *Optik* **39**(4), 416–436.

Rose H (1977). Nonstandard imaging methods in electron microscopy. *Ultramicroscopy* **2**(0), 251–267.

Rottmann PF & Hemker KJ (2018). Nanoscale elastic strain mapping of polycrystalline materials. *Mater Res Lett* **6**(4), 249–254.

Rouviere J-L, Béché A, Martin Y, Denneulin T & Cooper D (2013). Improved strain precision with high spatial resolution using nanobeam precession electron diffraction. *Appl Phys Lett* **103**(24), 241913.

Rozeveld S & Howe J (1993). Determination of multiple lattice parameters from convergent-beam electron diffraction patterns. *Ultramicroscopy* **50**(1), 41–56.

Ryll H, Simson M, Hartmann R, Holl P, Huth M, Ihle S, Kondo Y, Kotula P, Liebel A, Müller-Caspary K, *et al.* (2016). A pnCCD-based, fast direct single electron imaging camera for TEM and STEM. *J Instrum* **11**(04), P04006.

Schaffer B, Gspan C, Grogger W, Kothleitner G & Hofer F (2008). Hyperspectral imaging in TEM: New ways of information extraction and display. *Microsc Microanal* **14**(S2), 70–71.

Schwarzer R (1990). Measurement of local textures with transmission and scanning electron microscopes. *Texture, Stress, Microstruct* **13**(1), 15–30.

Schwarzer RA & Sukkau J (1998). Automated crystal orientation mapping (ACOM) with a computer-controlled TEM by interpreting transmission Kikuchi patterns. *Mater Sci Forum* **273**, 215–222.

https://doi.org/10.1017/S1431927619000497 Published online by Cambridge University Press

Schwarzhuber F, Melzl P, Pöllath S & Zweck J (2018). Introducing a non-pixelated and fast centre of mass detector for differential phase contrast microscopy. *Ultramicroscopy* **192**, 21–28.

Seyring M, Song X & Rettenmayr M (2011). Advance in orientation microscopy: Quantitative analysis of nanocrystalline structures. *ACS Nano* **5**(4), 2580–2586.

Shibata N, Findlay SD, Kohno Y, Sawada H, Kondo Y & Ikuhara Y (2012). Differential phase-contrast microscopy at atomic resolution. *Nat Phys* **8**(8), 611.

Shukla AK, Ophus C, Gammer C & Ramasse Q (2016). Study of structure of Li-and Mn-rich transition metal oxides using 4D-STEM. *Microsc Microanal* **22**(S3), 494–495.

Shukla AK, Ramasse QM, Ophus C, Kepaptsoglou DM, Hage FS, Gammer C, Bowling C, Gallegos PAH & Venkatachalam S (2018). Effect of composition on the structure of lithium-and manganese-rich transition metal oxides. *Energy Environ Sci* **11**(4), 830–840.

Song B, Ding Z, Allen CS, Sawada H, Zhang F, Pan X, Warner J, Kirkland AI & Wang P (2018). Hollow electron ptychographic diffractive imaging. *Phys Rev Lett* **121**(14), 146101.

Sourty E, Stanley J & Freitag B (2009). Using stem with quasi-parallel illumination and an automated peak-finding routine for strain analysis at the nanometre scale. *Physical and Failure Analysis of Integrated Circuits,* 2009. *IPFA* 2009. 16*th IEEE International Symposium on the*, 479–484.

Spence J (1998). Direct inversion of dynamical electron diffraction patterns to structure factors. *Acta Crystallogr, Sect A* **54**(1), 7–18.

Steeds J (1979). Convergent beam electron diffraction. In *Introduction to Analytical Electron Microscopy*. Boston, MA, USA: Springer, pp. 387–422.

Stevens A, Yang H, Hao W, Jones L, Ophus C, Nellist PD & Browning ND (2018). Subsampled STEM-ptychography. *Appl Phys Lett* **113**(3), 033104.

Sunde JK, Marioara CD, van Helvoort AT & Holmestad R (2018). The evolution of precipitate crystal structures in an Al-Mg-Si (-Cu) alloy studied by a combined HAADF-STEM and SPED approach. *Mater Charact* **142**, 458–469.

Tao J, Niebieskikwiat D, Varela M, Luo W, Schofield M, Zhu Y, Salamon MB, Zuo J-M, Pantelides ST & Pennycook SJ (2009). Direct imaging of nanoscale phase separation in $La_{0.55}Ca_{0.45}MnO_3$: Relationship to colossal magnetoresistance. *Phys Rev Lett* **103**(9), 097202.

Tao J, Sun K, Yin W-G, Wu L, Xin H, Wen J, Luo W, Pennycook S, Tranquada J & Zhu Y (2016). Direct observation of electronic-liquid-crystal phase transitions and their microscopic origin in $La_{1/3}Ca_{2/3}MnO_3$. *Sci Rep* **6**, 37624.

Tate MW, Purohit P, Chamberlain D, Nguyen KX, Hovden R, Chang CS, Deb P, Turgut E, Heron JT, Schlom DG, Ralph DC, Fuchs GD, Shanks KS, Philipp HT, Muller DA & Gruner SM (2016). High dynamic range pixel array detector for scanning transmission electron microscopy. *Microsc Microanal* **22**(1), 237–249.

Thibault P & Menzel A (2013). Reconstructing state mixtures from diffraction measurements. *Nature* **494**(7435), 68.

Tian L & Volkert C (2018). Measuring structural heterogeneities in metallic glasses using transmission electron microscopy. *Metals (Basel)* **8**(12), 1085.

Treacy M & Gibson J (1996). Variable coherence microscopy: A rich source of structural information from disordered materials. *Acta Crystallogr, Sect A* **52**(2), 212–220.

Trimby PW (2012). Orientation mapping of nanostructured materials using transmission Kikuchi diffraction in the scanning electron microscope. *Ultramicroscopy* **120**, 16–24.

Uesugi F, Hokazono A & Takeno S (2011). Evaluation of two-dimensional strain distribution by STEM/NBD. *Ultramicroscopy* **111**(8), 995–998.

Usuda K, Mizuno T, Tezuka T, Sugiyama N, Moriyama Y, Nakaharai S & Takagi S (2004). Strain relaxation of strained-Si layers on SiGe-on-insulator (SGOI) structures after mesa isolation. *Appl Surf Sci* **224**, 113–116.

Vigouroux M, Delaye V, Bernier N, Cipro R, Lafond D, Audoit G, Baron T, Rouvière J, Martin M, Chenevier B, *et al.* (2014). Strain mapping at the nanoscale using precession electron diffraction in transmission electron microscope with off axis camera. *Appl Phys Lett* **105**(19), 191906.

Vincent R & Midgley P (1994). Double conical beam-rocking system for measurement of integrated electron diffraction intensities. *Ultramicroscopy* **53**(3), 271–282.

Voyles P & Muller D (2002). Fluctuation microscopy in the STEM. *Ultramicroscopy* **93**(2), 147–159.

Waddell E & Chapman J (1979). Linear imaging of strong phase objects using asymmetrical detectors in stem. *Optik* **54**(2), 83–96.

Wang F, Pennington RS & Koch CT (2016). Inversion of dynamical scattering from large-angle rocking-beam electron diffraction patterns. *Phys Rev Lett* **117**(1), 015501.

Wang P, Zhang F, Gao S, Zhang M & Kirkland AI (2017). Electron ptychographic diffractive imaging of boron atoms in LaB_6 crystals. *Sci Rep* **7**(1), 2857.

Wang Y, Suyolcu YE, Salzberger U, Hahn K, Srot V, Sigle W & van Aken PA (2018). Correcting the linear and nonlinear distortions for atomically resolved STEM spectrum and diffraction imaging. *Microscopy* **67**(suppl_1), i114–i122.

Watanabe M & Williams D (2007). Development of diffraction imaging for orientation analysis of grains in scanning transmission electron microscopy. *Microsc Microanal* **13**(S02), 962–963.

Webb RH (1996). Confocal optical microscopy. *Rep Prog Phys* **59**(3), 427.

Wehmeyer G, Bustillo KC, Minor AM & Dames C (2018). Measuring temperature-dependent thermal diffuse scattering using scanning transmission electron microscopy. *Appl Phys Lett* **113**(25), 253101.

Williamson M, van Dooren P & Flanagan J (2015). Quantitative analysis of the accuracy and sensitivity of strain measurements from nanobeam electron diffraction. *IEEE* 22*nd International Symposium on the Physical and Failure Analysis of Integrated Circuits* (*IPFA*), 197–200.

Wright SI, Nowell MM & Field DP (2011). A review of strain analysis using electron backscatter diffraction. *Microsc Microanal* **17**(3), 316–329.

Xu W & LeBeau JM (2018). A deep convolutional neural network to analyze position averaged convergent beam electron diffraction patterns. *Ultramicroscopy* **188**, 59–69.

Yadav AK, Nguyen KX, Hong Z, Garcia-Fernandez P, Aguado-Puente P, Nelson CT, Das S, Prasad B, Kwon D, Cheema S, Khan AI, Hu C, Iniguez J, Junquera J, Chen L-Q, Muller DA, Ramesh R & Salahuddin S (2019). Spatially resolved steady-state negative capacitance. *Nature* **565**, 468–471.

Yang H, Jones L, Ryll H, Simson M, Soltau H, Kondo Y, Sagawa R, Banba H, MacLaren I & Nellist P (2015*a*). 4D STEM: High efficiency phase contrast imaging using a fast pixelated detector. *J Phys Conf Ser* **644**(1), 012032.

Yang H, Pennycook TJ & Nellist PD (2015*b*). Efficient phase contrast imaging in STEM using a pixelated detector. Part II: Optimisation of imaging conditions. *Ultramicroscopy* **151**, 232–239.

Yang H, Ercius P, Nellist PD & Ophus C (2016*a*). Enhanced phase contrast transfer using ptychography combined with a pre-specimen phase plate in a scanning transmission electron microscope. *Ultramicroscopy* **171**, 117–125.

Yang H, Rutte R, Jones L, Simson M, Sagawa R, Ryll H, Huth M, Pennycook T, Green M, Soltau H, *et al.* (2016*b*). Simultaneous atomic-resolution electron ptychography and Z-contrast imaging of light and heavy elements in complex nanostructures. *Nat Commun* **7**, 12532.

Yang H, MacLaren I, Jones L, Martinez GT, Simson M, Huth M, Ryll H, Soltau H, Sagawa R, Kondo Y, *et al.* (2017). Electron ptychographic phase imaging of light elements in crystalline materials using Wigner distribution deconvolution. *Ultramicroscopy* **180**, 173–179.

Yankovich AB, Berkels B, Dahmen W, Binev P, Sanchez SI, Bradley SA, Li A, Szlufarska I & Voyles PM (2014). Picometre-precision analysis of scanning transmission electron microscopy images of platinum nanocatalysts. *Nat Commun* **5**, 4155.

Yasin FS, Harada K, Shindo D, Shinada H, McMorran BJ & Tanigaki T (2018*a*). A tunable path-separated electron interferometer with an amplitude-dividing grating beamsplitter. *Appl Phys Lett* **113**(23), 233102.

Yasin FS, Harvey TR, Chess JJ, Pierce JS & McMorran BJ (2018*b*). Path-separated electron interferometry in a scanning transmission electron microscope. *J Phys D: Appl Phys* **51**(20), 205104.

Yasin FS, Harvey TR, Chess JJ, Pierce JS, Ophus C, Ercius P & McMorran BJ (2018*c*). Probing light atoms at subnanometer resolution: Realization of scanning transmission electron microscope holography. *Nano Lett* **18**(11), 7118–7123.

Zaefferer S (2000). New developments of computer-aided crystallographic analysis in transmission electron microscopy. *J Appl Crystallogr* **33**(1), 10–25.

Zaefferer S (2011). A critical review of orientation microscopy in SEM and TEM. *Cryst Res Technol* **46**(6), 607–628.

https://doi.org/10.1017/S1431927619000497 Published online by Cambridge University Press

Zaluzec NJ (2002). Quantitative measurements of magnetic vortices using position resolved diffraction in Lorentz STEM. *Microsc Microanal* **8**(S02), 376–377.

Zaluzec NJ (2003). Computationally mediated experimental science. *Microsc Microanal* **9**(S02), 150–151.

Zaluzec N (2007). Scanning confocal electron microscopy. *Microsc Microanal* **13**(S02), 1560–1561.

Zeng Z, Zhang X, Bustillo K, Niu K, Gammer C, Xu J & Zheng H (2015). *In situ* study of lithiation and delithiation of MoS_2 nanosheets using electrochemical liquid cell transmission electron microscopy. *Nano Lett* **15**(8), 5214–5220.

Zhang P, Istratov AA, Weber ER, Kisielowski C, He H, Nelson C & Spence JC (2006). Direct strain measurement in a 65 nm node strained silicon transistor by convergent-beam electron diffraction. *Appl Phys Lett* **89**(16), 161907.

Zhang H, Ning H, Busbee J, Shen Z, Kiggins C, Hua Y, Eaves J, Davis J, Shi T, Shao Y-T, *et al.* (2017). Electroplating lithium transition metal oxides. *Sci Adv* **3**(5), e1602427.

Zheng C & Etheridge J (2013). Measurement of chromatic aberration in STEM and SCEM by coherent convergent beam electron diffraction. *Ultramicroscopy* **125**, 49–58.

Zheng C, Zhu Y, Lazar S & Etheridge J (2014). Fast imaging with inelastically scattered electrons by off-axis chromatic confocal electron microscopy. *Phys Rev Lett* **112**(16), 166101.

Zhu G-Z, Radtke G & Botton GA (2012). Bonding and structure of a reconstructed (001) surface of $SrTiO_3$ from TEM. *Nature* **490**(7420), 384.

Zuo J (1992). Automated lattice parameter measurement from HOLZ lines and their use for the measurement of oxygen content in $YBa_2Cu_3O_{7-\delta}$ from nanometer-sized region. *Ultramicroscopy* **41**(1–3), 211–223.

https://doi.org/10.1017/S1431927619000497 Published online by Cambridge University Press